

Apical oxygen vibrations dominant role in d-wave cuprate superconductivity and its interplay with spin fluctuations.

B. Rosenstein¹ and B. Ya. Shapiro²

¹*Department of Electrohysics, National Yang Ming Chiao Tung University, Hsinchu, Taiwan, R.O.C.*

²*Department of Physics, Institute of Superconductivity, Bar-Ilan University, 52900 Ramat-Gan, Israel.*

Microscopic theory of a high T_c cuprate $Bi_2Sr_2CaCu_2O_{8+x}$ based on main pairing channel of electrons in CuO planes due to 40mev lateral vibrations of the apical oxygen atoms in adjacent the SrO ionic insulator layer is proposed. The separation between the vibrating charged atoms and the 2D electron gas creates the forward scattering peak leading in turn to the d-wave pairing within Eliashberg formalism. The phonon mode naturally explain the kink in dispersion relation observed by ARPES and the and effect of the $O^{16} \rightarrow O^{18}$ isotope substitution in the normal state. To describe the pseudogap physics a single band fourfold symmetric $t-t'$ Hubbard model, with the hopping parameters $t' \sim -0.17t$ and the on site repulsion $e U \sim 6t$. It described the Mott insulator at low doping, while at higher dopping the pseudogap physics (still strongly correlated) can be be approximated by the symmetrized mean field model and with renormalized U incorporating screening. The location of the transition line T^* between the locally antiferromagnetic pseudogap and the paramagnetic overdoped phases and susceptibility (describing spin fluctuations coupling to 2DEG) are also obtained within this approximation. The superconducting d -wave gap mainly due to the phonon channel but is assisted by the spin fluctuations (15-20%). The dependence of the gap and T_c on doping and effect of the isotope substitution are obtained and is consistent with experiments.

PACS numbers: PACS: 74.20.Mn, 74.20.Rp, 74.72.Hs

I. INTRODUCTION.

For decades the only superconductors with critical temperature above $90K$ under ambient conditions were cuprates like $Bi_2Sr_2CaCu_2O_{8+x}$ ($Bi2212$). They are generally characterized by the following five structural/chemical/electronic peculiarities. First, they are all quasi - two dimensional (2D) perovskite layered oxides. Second, the 2D electron gas (2DEG) in which the superconductivity resides is created by "charging" CuO planes: hole doping the anti - ferromagnetic (AF) parent material. Third, the conducting layers are separated by several insulating ionic oxide planes. Fourth, as doping decreases past optimal the pseudogap is opened and closed Fermi surface splits into four arcs¹ (a topological transition). Fifth is the d - wave symmetry of the order parameter below the "superconducting dome" on the phase diagram. It is widely believed² that, although the insulating layers play a role in charging the CuO planes, the (still not clearly identified) bosons responsible for the pairing (so called "glue") are confined to the CuO layer.

Several years ago another group of superconducting materials with critical temperature as high as $T_c = 60 - 106K$ was fabricated by deposition of a single unit cell layer (1UC) of $FeSe$ on insulating substrates like $SrTiO_3$ (STO both³ (001) and⁴ (110)), TiO_2 and⁵ $BaTiO_3$. Note that the first three of the characteristic cuprate features listed above are manifest in these systems as well. Indeed, the insulating substrates are again the perovskite oxide planes. The electron gas residing in the $FeSe$ layer⁶ is charged (doped) by the perovskite substrate. The remaining two of the five cuprate features are clearly distinct in the new superconductor family. The Fermi surface is nearly round in sharp contrast to the rhomb - shaped one in cuprates. There are neither pseudogap nor the electron "pockets". Furthermore the symmetry of the order parameter is the nodules s - wave⁷. Generally the system is much simpler than the cuprates and much progress in understanding of its superconductivity mechanism was achieved. The role of the insulating substrate in $FeSe/STO$ seems to extend beyond the charging⁶. While the physical nature of the pairing boson in cuprates is still under discussion, it became clear that superconductivity mechanism in 1UC $FeSe/STO$ should at least include the *substrate* phonon exchange. Although there are theories based on an unconventional boson exchange *within* the pnictides plane (perhaps spin fluctuations exchange⁸, as in pnictides theories⁹), an alternative point of view was clearly formed^{10,11} based on idea that the pairing in the $FeSe$ plane is largely due to vibration of oxygen atoms in a substrate oxide layer near the interface.

Historically a smoking gun for the relevance of the electron - phonons interactions (EPI) to superconductivity has been the isotope effect. When the isotope ^{16}O in surface layers of the STO substrate was substituted¹² by ^{18}O , the gap at low temperature ($6K$) decreased by about 10%. Detailed measurements of the phonon spectrum via electron energy loss spectroscopy¹³ demonstrated that the interface phonons are very energetic (the "hard" longitudinal optical (LO) branch appears at $\Omega_h = 100mev$). The phonons couple to 2DEG with relatively small coupling constant¹² $\lambda \simeq 0.25$, deduced from the intensity of the replica bands identified by ARPES¹⁴. Importantly the interpretation of the replica bands was based on the forward peak in the electron - phonon scattering (FSP). Initially this inspired an idea that the surface phonons alone could provide a sufficiently strong pairing¹¹. Since the BCS scenario, $T_c \approx \Omega_h e^{-1/\lambda}$, is clearly out, one had to look for other ideas like the extreme, delta like, FSP model^{15,16} for which $T_c \approx \frac{\lambda}{2+3\lambda} \Omega_h$. This lead¹¹ to sufficiently high T_c for small λ . Unfortunately the EPI parameters to achieve such a strong FSP in ionic substrate are unrealistic. In a recent work¹⁷ we developed a sufficiently precise microscopic model of phonons in adjacent insulating TiO_2 layer of the STO substrate and found an additional $\Omega_s = 50mev$ LO interface phonon. Since coupling of the Ω_s to the electron gas in the $FeSe$ layer is practically the same as that of the hard Ω_h mode, it greatly enhances pairing. The momentum dependence of the EPI matrix elements has an exponential FSP, $exp[-2pd_a]$, where d_a is the distance between the ionic layer and 2DEG. Calculated coupling λ , critical temperature, replica band and other characteristics of the superconducting state are consistent with experiments. It demonstrated that the perovskite ionic layer phonons constitute a sufficiently strong "glue" to mediate high T_c superconductivity.

A question arises whether similar phononic pairing mechanism occurs in cuprates. Of course there is a structural difference between the cuprates and the 1UC $FeSe/STO$ in that the the bulk layered cuprates contain many CuO planes, while there is a single $FeSe$ layer. The difference turns out to be insignificant, since it was demonstrated^{18,19} that even two unit cells of optimally doped $Bi2212$ sandwiched between insulating materials exhibits practically as high T_c as the bulk material. Also recently a CuO monolayer on top of $Bi2212$ film was synthesized²⁰ with surprisingly high the critical temperature of $100K$. The pairing is of a nodules s-wave variety as in 1UC $FeSe/STO$ in striking contrast with $Bi2212$ and other hole doped cuprates. The s - wave symmetry was explained by extremely strong charging^{20,21}. In particular it was noticed that the Fermi surface becomes nearly *circular*²¹ also in sharp contrast to the rhombic shape of hole doped cuprates.

The idea that phonons are at least partially responsible for the d - wave pairing has been contemplated over the years. In particular the CuO layer oxygen atoms breathing and buckling modes²² and the apical oxygen c axis vibrations^{23,24,25} have been considered. It is well established that phonons cause s - wave pairing in low T_c materials, d-wave pairing is possible when FSP is present. It turns out that the nature of pairing for the FSP phonons depend on the shape of the Fermi surface, assumed to be fourfold symmetric throughout this paper. Our experience can be

summarizes as follows. The pairing tends to be d-wave for a rhomb-like Fermi surface and s-wave for a more circular one like that of 1UC $FeSe/STO$ or $CuO/Bi2212$. Early work in this direction was summarized in ref.¹⁵. It was found that at weak coupling the Lorentzian FSP led to increase of T_c , while at strong coupling the phonon contribution was detrimental due to large renormalization parameter. Consensus emerged that the EPI of CuO plane phonons alone is not strong enough to get such a high T_c . EPI exchange can somewhat enhance, but cannot be the major cause of the d-wave pairing.

In view of the experience with 1UC $FeSe/STO$, it is natural to ask whether the lateral apical oxygen phonon exchange that *naturally has* exponential FSP, due to distance d_a between the conducting and insulating layers, can lead to the *d-wave* pairing in cuprates. It immediately reminds a high T_c "smoking gun" that was observed of more than a decade ago. It was discovered²⁵ that the superconducting gap in $Bi2212$ is (locally) anti-correlated precisely to the distance, d_a , between the Cu atoms and the apical oxygen atoms just below/above. This is the first "smoking gun" pointing at crucial role of the apical oxygen atoms. The evidence of the anti-correlation is not conclusive since recently correlation single-layer $Bi_2Sr_{0.9}La_{1.1}CuO_6$, double-layer $Nd_{1.2}Ba_{1.8}Cu_3O_6$ and infinite-layer $CaCuO_2$ was observed²⁶.

The second smoking gun is the tunneling experiment²⁷ that the authors describe best: "We find intense disorder of electron-boson interaction energies at the nanometer scale, along with the expected modulations in d^2I/dV^2 . Changing the density of holes has minimal effects on both the average mode energies and the modulations, indicating that the bosonic modes are unrelated to electronic or magnetic structure. Instead, the modes appear to be local lattice vibrations, as substitution of ^{18}O for ^{16}O throughout the material reduces the average mode energy by approximately 6% - the expected effect of this isotope substitution on lattice vibration frequencies." This is an indication that vibrating oxygen atoms are out of the CuO plane. We therefore revisit this clear evidence in light of the lateral apical vibration superconductivity theory.

Unlike 1UC CuO , where no measurements of the phonon excitations were made to date, the bulk $BSCCO$ crystals were thoroughly studied. Evidence consists of the "kink" in quasiparticle dispersion relation in normal state²⁸⁻³⁰ measured by ARPES, large isotope effect observed mainly in underdoped samples³¹ and the statistics of the STM measurements²⁷. The kinks should be attributed to EPI, since their locations (energies) change³⁰ by 6% upon substitution of the ^{16}O isotope by ^{18}O . The distribution of d^2I/dV^2 is independent of doping in a wide range. In particular its average value is 40meV and is shifted by 6% upon the isotope substitution²⁷. This indicates that if the phonon pairing mechanism is dominant the relevant phonons do not belong to the CuO planes. Phonons in cuprates were extensively studied within the microscopic (DFT) approach including the oxygen vibration mode³².

In the present paper we construct a theory of a high T_c cuprate that based on the idea of dominant pairing due to *apical lateral longitudinal phonons* (ALLP) along with minor AF fluctuations contribution. This 40meV phonon mode and its coupling including the matrix elements are described sufficiently well by the Born-Meyer approximation^{33,34} that has been applied to cuprates³⁵. To support the pairing scenario, it is crucial to present a simple enough microscopic model of cuprates that comprehensively describes (at least qualitatively) various features of the material over the whole doping-temperature phase diagram (underdoped to overdoped) including both normal and d-wave superconducting states. To be more specific we consider the effect of the ALLP pairing in the arguably best studied cuprate superconductor $Bi2212$. To describe the pseudogap physics of 2DEG in the CuO planes we limit ourselves to the fourfold symmetric $t-t'$ single band Hubbard model² with on-site repulsion energy U . In the absence of direct experimental determinations of U , one resorts to the first principle calculations. Most of the microscopic (DFT) determinations of U ³⁶ are in the "strong coupling Mott insulator" range $U/t = 5-10$, so that U is comparable to the bandwidth W . Recently however in a similar type of the first principle calculations³⁷ resulted in smaller values of U . It turns out within our approach that in order to describe the pseudogap physics, parameters of the model are restricted to a rather narrow "window" around $t' \sim -0.2t$, $U \sim 6t$. Since the ALLP exchange is effective enough to be the dominant "glue" responsible for the d-wave pairing, a simple description of the Hubbard model combining the RPA type coupling renormalization due to screening³⁸ and the symmetrized HF approach³⁹ is sufficiently accurate. The spin fluctuations exchange enhances superconductivity by 15-20%.

Two conditions turned out to be sufficient to trigger robust apical phonon d-wave pairing: the rhombic shape of the Fermi surface and the exponential FSP of the ALLP mode. The dependence of the superconducting gap on doping, temperature and effect of the $^{16}O \rightarrow ^{18}O$ isotope substitution are obtained. In normal state the dimensionless EPI strength is $\lambda \sim 0.6$, thus justifying the use of the weak coupling approach⁴⁰. The phonons naturally explain the effect of the isotope substitution on the kink in dispersion relation.

The paper is organized as follows. In Section II a sufficiently precise phenomenological model of the lateral optical phonons in ionic crystal is developed. In Section III an effective model of the correlated electron gas is presented. Section IV is devoted to normal state properties: the pseudogap phenomena (including the T^* line, fragmentation of the quasi-particle spectrum) and renormalization of the electron Green's function due to phonons. This allows location of kink in dispersion relation (including the isotope dependence) and the EPI coupling λ . In Section V superconductivity is studied in the framework of dynamic Eliashberg approach. Both the phonon and the spin

fluctuation channels are accounted for over the full doping range. The isotope effect exponent is determined. In the last Section results are summarized and discussed. A simplified general picture of the d - wave pairing by apical phonons and its coexistence with spin fluctuations is presented.

II. THE MODEL

Our model consists of the 2DEG interacting with phonons of a polar insulator:

$$H = H_{Hub} + H_{ph} + H_{e-ph}. \quad (1)$$

We start with the phonon. The electron part is the Hubbard model, while the coupling between the electronic and vibrational degrees of freedom, H_{e-ph} , is subject of the last Subsection.

A. What phonons are contributing most to the electron - electron pairings?

Although the prevailing hypothesis is that superconductivity in cuprate is "unconventional", namely not to be phonon - mediated, the phonon based mechanism has always been a natural option to explain extraordinary superconductivity in cuprates. As mentioned in Introduction, the most studied phonon glue mode has been the oxygen vibrations within the CuO plane²²⁴¹¹⁵¹⁶. As argued in ref.¹⁷, in the context of high T_c 1UC $FeSe$ on perovskite substrates, lateral vibrations of the oxygen atoms in the adjacent ionic perovskite layer can couple sufficiently strongly to 2DEG residing in the CuO plane to be a viable option. Qualitatively one of the reasons is that the SrO layer constitutes a strongly coupled ionic insulator. Unlike the metallic layer where screening is strong, in an ionic layer screening is practically absent and a simple microscopic theory of phonons and their coupling exists³³. It was repeatedly noticed¹⁰ that vibrations in c directions contribute little to pairing. Let us start with a brief description of the structure of the perhaps best studied high T_c material $Bi2212$. Then the microscopic lateral vibrations model is presented, while their coupling to the electron gas is considered in the next Section.

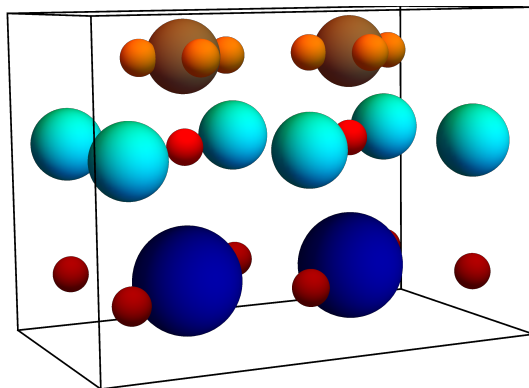


FIG. 1. The profile 3D view of three layers comprising relevant part of the one unit cell "molecule" of $Bi2212$. Top (2DEG) layer: Cu (brown) O_2 (orange), the apic phonon layer: Sr (cyan) O (red). The third layer: Bi (violet) O (dark red). Sizes of atoms are inversely proportional to the values of the Born - Mayer inter - atomic potential parameter b in Eq.(2).

The structure of the quarter of the $Bi_2Sr_2CaCu_2O_{8+\delta}$ unit cell near the conducting layer is schematically depicted in Fig. 1. Electronic properties in both normal and superconducting states of cuprates are determined by holes (created by doping) in conducting CuO layers, see top layer in Fig.1 (where Cu is drawn as a brown sphere, O - small orange spheres) and the left most chart in Figs. 8 (Appendix A). Besides the single CuO_2 layer only two insulating oxide layers are assumed to be relevant. The closest layer at distance $d_a = 1.84A$, see the second chart from left in Fig.8a, consists of heavy Sr atoms (cyan rings) and light "apical" oxygen (small red circle). The next layer is BiO , see the third chart from left in figure in Fig. 8b (Bi - violet large ring, O - small dark red circles). Below this layer the pattern is replicated in reverse order. Of course $Bi2212$ has metallic bilayers separated by Ca . In this paper we neglect the effects of tunneling between the CuO_2 layers. Out of plane spacings counted from the SrO layer are specified in Table I.

TABLE I. Atomic parameters determining lateral apical oxygen vibrations.

atom	<i>Cu</i>	<i>O</i> ₁	<i>Sr</i>	<i>O</i> ₂	<i>Bi</i>	<i>O</i> ₃
mass (a.u.)	64	16	88	16	209	16
<i>A</i> (keV)	13.919	2.143	20.785	2.143	63.922	2.143
<i>b</i> (Å ⁻¹)	3.561	3.788	3.541	3.788	3.4998	3.788
charge <i>Z</i>	2.4	-1.2	.95	-.95	1.33	-1.33
spacing <i>z</i> (Å)	1.84	1.84	0	0	-2.75	-2.75

The translational symmetry in the lateral (*x,y*) directions of the system has the lattice spacing of $a = 3.9\text{\AA}$ and coincides with the distance between the *Cu* atoms. Distances between the layers are also given Table I neglecting small canting. The crystal has very rich spectrum of phonon modes. However very few have a strong coupling to 2DEG and even fewer can generate lateral (in plane) forces causing pairing. While phonons within the *CuO* planes have been extensively studied both theoretically^{15,22} and experimentally, the conclusion is that they do not constitute a strong enough "glue". It is reasonable to expect that the modes most relevant for the electron - phonon coupling are the vibrations of the atoms in the adjacent *SrO* layer, see Fig.1. This is in conformity with the first and second "smoking gun" experiment findings^{25,27}: the "glue" is independent of the doping and anything else that happens in the 2DEG in the *CuO*₂ layer simply because the phonons are originating in different layer.

B. Lateral apical oxygen optical phonon modes in the *SrO* layer.

Phonons in ionic crystals are described by the Born - Meyer potential due to electron's shells repulsion³³ and electrostatic interaction of ionic charge,

$$V^{XY}(r) = \sqrt{A_X A_Y} \exp\left[\frac{1}{2}(b^X + b^Y)r\right] + Z_X Z_Y \frac{e^2}{r}, \quad (2)$$

with values of coefficients *A* and *b* listed in Table I. The ionic charges *Z* are estimated from the DFT calculated Milliken charges³⁴. In the *SrO* layer the charges are constrained by neutrality. Since oxygen is much lighter than *Sr*, the heavy atoms' vibrations are negligible. Obviously that way we lose the acoustic branch, however it is known that the acoustic phonons contribute little to the pairing^{10,42}. Atoms in neighboring layers can also be treated as static. Moreover one can neglect more distant layers. Even the influence of the lower *BiO* layer (below the last layer shown in Fig.1) is insignificant due to the distance. Consequently the dominant lateral displacements, $u_{\mathbf{m}}^\alpha$, $\alpha = x, y$, are of the oxygen atoms directly beneath the *Cu* sites at $\mathbf{r}_{\mathbf{m}} = a(m_1, m_2)$.

The dynamic matrix $D_{\mathbf{q}}^{\alpha\beta}$ is calculated by expansion of the energy to second order in oxygen displacement (details in Appendix A), so that the phonon Hamiltonian in harmonic approximation is:

$$H_{ph} = \frac{1}{2} \sum_{\mathbf{q}} \left\{ M \frac{du_{-\mathbf{q}}^\alpha}{dt} \frac{du_{\mathbf{q}}^\alpha}{dt} + u_{-\mathbf{q}}^\alpha D_{\mathbf{q}}^{\alpha\beta} u_{\mathbf{q}}^\beta \right\}. \quad (3)$$

Here *M* is the oxygen mass. Summations over repeated components indices is implied. Now we turn to derivation of the phonon spectrum. Two eigenvalues, the transversal (red) optical (TO) and the longitudinal (blue) optical (LO) modes are given in Fig. 2. One observes that there are longitudinal modes are in the range $\Omega_{\mathbf{q}} \sim 26 - 41\text{meV}$ and $22 - 32\text{meV}$ respectively. The energy of LO modes is larger than that of the corresponding TO, although the sum $\Omega_{\mathbf{q}}^{LO} + \Omega_{\mathbf{q}}^{TO}$ is nearly dispersionless. At Γ the splitting is small, while due to the long range Coulomb interaction there is hardening of LO and softening of TO at the BZ edges. The dispersion of the high frequency modes is small, while for the lower frequency mode it is more pronounced.

C. The *t - t'* Hubbard model of the 2DEG in *CuO* layers.

The electron gas of *Bi2212* consists of two identical layers with tunneling between them. The effective single band model. Neglecting the inter - layer tunneling, the simplest *t - t'* Hamiltonian in momentum space is:

$$K = \sum_{\mathbf{k}} c_{\mathbf{k}}^{\sigma\dagger} (\epsilon_{\mathbf{k}} + \epsilon'_{\mathbf{k}} - \mu) c_{\mathbf{k}}^{\sigma}, \quad (4)$$

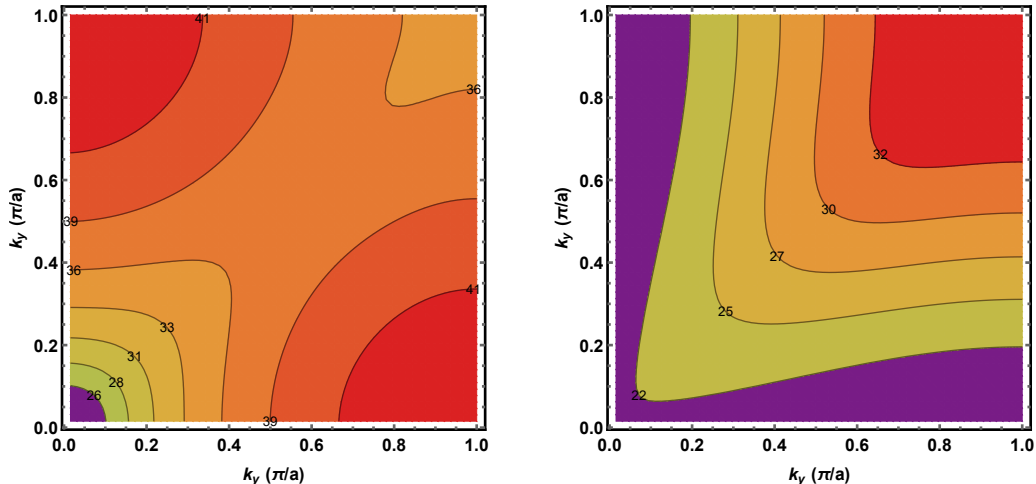


FIG. 2. Spectrum of the lateral apical oxygen vibrations in the SrO plane. a. longitudinal optical modes, b. transverse optical modes. Note moderate dispersion of the longitudinal mode.

Here $c_{\mathbf{k}}^{\sigma\dagger}$ is the electron creation operator with spin projection $\sigma = \uparrow, \downarrow$. Only nearest and next to nearest neighbors hopping terms are included:

$$\begin{aligned} \epsilon_{\mathbf{k}} &= -2t (\cos [ak_x] + \cos [ak_y]); \\ \epsilon'_{\mathbf{k}} &= -4t' \cos [ak_x] \cos [ak_y]. \end{aligned} \quad (5)$$

Summations are always over the 2D Brillouin zone, $-\pi/a < k_x, k_y < \pi/a$. The dispersion relation thus is simplified with respect to a "realistic" one^{43,44} in which splitting due to tunneling is also taken into account and more distant hops are included. Values of the hopping parameters, see Table II will be fixed independently of chemical potential μ determining the (hole) doping x . Reasons for such a choice will be given after the phase diagram will be presented in the next Section.

The on site repulsion is described by the on site Hubbard repulsion term²

$$V = U \sum_{\mathbf{i}} n_{\mathbf{i}}^{\uparrow} n_{\mathbf{i}}^{\downarrow}, \quad (6)$$

with $n_{\mathbf{i}}^{\sigma} = c_{\mathbf{i}}^{\sigma\dagger} c_{\mathbf{i}}^{\sigma}$ being the spin σ occupation on the site $\{i_x, i_y\}$. Due to strong repulsion, even the model without phonons is highly nontrivial and will be treated approximately in the next Section. Now we turn to the electron - phonon coupling.

While the lattice spacing a is firmly determined by experiment (and is nearly independent of doping for small x), the microscopic⁴⁵ or phenomenological⁴³ estimates for other electron gas parameters like the energy scales U, t, t', μ vary considerably in different one band Hubbard approaches. The values of $t = 0.3eV$, $U = 6$ at zero doping will be used throughout the paper to fit numerous experimental quantities like the ARPES⁴³, the pseudogap characteristics⁴⁴. The range of acceptable values of t'/t is rather limited. If one chooses $|t'|/t < 0.12$, the Mott state at very low doping does not appear⁴⁶. At values larger than $|t'|/t > 0.25$ the shape of the Fermi surface in the underdoped regime is qualitatively different from the one observed by ARPES⁴⁷. The value of $t' = -0.17t$ is chosen to tune the Lifshitz (topological) transition from the full Fermi surface to the fractured one (four arcs) occurs at experimentally observed¹⁸ doping $x^{opt} = 0.16$.

D. Electron - phonon coupling

The lateral apical oxygen phonon's interaction with the 2DEG on the adjacent CuO layer $d_a = 1.84A$ above the SrO plane is determined by the electric potential created the charged apical oxygen vibration mode $\mathbf{u}_{\mathbf{m}}$ at arbitrary point \mathbf{r} is:

$$\Phi(\mathbf{r}) = \sum_{\mathbf{m}} \frac{Ze}{\sqrt{(\mathbf{r} - \mathbf{r}_{\mathbf{m}} - \mathbf{u}_{\mathbf{m}})^2 + d_a^2}}, \quad (7)$$

Here the apical oxygen charge taken to be $Z = -0.95$, see Table I. This value is slightly below the charge at which transition to charge density wave occurs. The interaction electron-phonon Hamiltonian that accounts for the hole charge distribution in the CuO plane is derived in Appendix A. The result in momentum space has a density - displacement form

$$H_{eph} = Ze^2 \sum_{\mathbf{q}} n_{-\mathbf{q}} g_{\mathbf{q}}^{\alpha} u_{\mathbf{q}}^{A\alpha}, \quad (8)$$

with EPI matrix element,

$$\mathbf{g}_{\mathbf{q}} = \frac{1}{2} \left(\cos \frac{aq_x}{2} + \cos \frac{aq_y}{2} \right) \bar{\mathbf{g}}_{\mathbf{q}}; \quad \bar{\mathbf{g}}_{\mathbf{q}} \approx 2\pi e^{-qd_a} \frac{\mathbf{q}}{q}. \quad (9)$$

It is well known that only longitudinal phonons contribute to the effective electron - electron interaction, as is clear from the scalar product form of the Eq.(8). The precision of the last equality is 2%, see figure 9,10 in Appendix A.

To conclude Eqs.(4,3,8) define our microscopic model. Now we turn to description of the normal state properties of 2DEG, including the influence of the EPI.

III. NORMAL STATE PROPERTIES: PSEUDOGAP, EPI COUPLING STRENGTH AND KINK IN DISPERSION RELATION.

The normal state of cuprates exhibits a host of phenomena including pseudogap in underdoped regime resulting in fracture of the Fermi surface, significant charge and spin susceptibility due to strong anti - ferromagnetic correlations (leading to enhancement of the d - wave pairing). These phenomena are described in the framework of the strongly coupled Hubbard model defined in the previous Section. Unfortunately the theoretical description of the Hubbard model away from half filling (Monte Carlo⁴⁸, diagrammatic^{49,50}) is either uncertain or extremely complicated. We use a much simpler approximation scheme including the RPA type coupling U renormalization⁵¹ and symmetrized HF³⁹. It provides a good agreement with the more sophisticated methods. Coupling to phonons also affects the normal properties such as the dispersion relation. The strength of EPI will be estimated and the quasi - particle self energy calculated perturbatively.

A. Renormalized mean field description of the Hubbard model

Hubbard model at moderate value $U = 6$ in the doping range $x = 0.05 - 0.25$ range is a strongly correlated fermion system that does not allow the Landau liquid description (except at high doping). Generally it is also out of applicability range of the HF approximation due to large vertex corrections^{49,50}. However it is well known that the overdoped system has a well defined Fermi surface and can be very well described by the HF type two - body correlator⁴³. In the underdoped phase one obtains an effective description in terms of "RVB" correlators⁵² that have recently been cast as a symmetrized HF³⁹. Such an approach is consistent if the vertex corrections effectively lead to reduction of the coupling to a smaller value \bar{U} . It turns out that MC and diagrammatic results can be approximated by such a scheme when the renormalized \bar{U} ,

$$\bar{U} = \frac{U}{1 - \frac{U}{2} \chi_0}, \quad (10)$$

where χ_0 is the (Matsubara) charge susceptibility. This should be solved consistently with the HF equations and is described in both the overdoped and the underdoped phases in Appendix B.

The coupling $U = 6$ is reduced by screening to the renormalized values given in Table II. The HF equations were solved numerically by iterations on lattice $N = 128 \times 128$ with periodic boundary conditions.

One of the striking normal state phenomena in underdoped cuprates is pseudogap^{1,53}. In the present paper we adopt a point of view that pseudogap to the short range anti - ferromagnetic order within each of the CuO layers. The long

TABLE II. Effective (renormalized) coupling as function of doping for bare coupling $U = 6$ and $t'/t = -0.17$.

hole doping $x(\%)$	1	2	3	5	7	9	11	13	14	15	16	17	19	21	23	25	28
eff. coupling U_r	4.35	4.06	3.93	3.82	3.67	3.52	3.33	3.1	2.94	2.65	1.91	1.93	2.03	2.14	2.23	2.3	2.33

range AF order is lost at a relatively small doping and the system becomes quasi two dimensional. In 2D one can model the short range order and the fluctuations effects² by considering the macroscopic sample as a system of AF domains with certain domain size. Generally local (STM) probes described in Introduction provide distribution of quantities like pseudogap within the domains. On the other hand ARPES, thermodynamic and transport experiments provide information on all the scales, namely after averaging over the domains. It is found that the value of the pseudogap is qualitatively agree with somewhat similar calculations⁵⁴ (improved by the renormalization group), the MC simulations and experiments^{1,53}.

The transition temperature T^* as function of the hole doping, $x = 1 - n$, is given in Fig. 3 as the green line. It starts at the quantum critical point $x^* = 0.16$, rapidly increases (almost vertically although a slight bending is visible) intersecting with the superconducting transition temperature T_c . Then it curves towards the AF phase at small doping. The mean field transition happens to be second order with an exception of the small section below the "superconducting dome" in Fig. 3 (marked by a phenomenological parabolic fit to experiment, see ref.¹⁸).

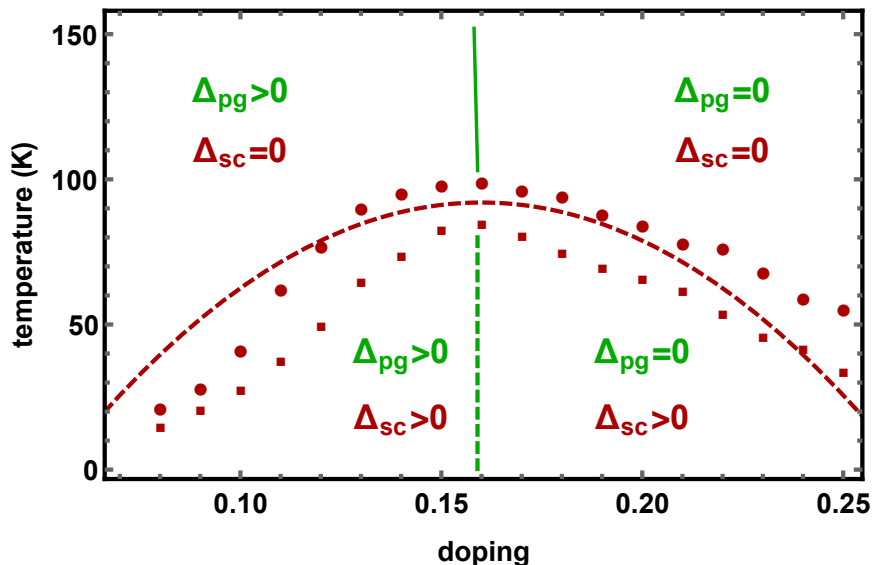


FIG. 3. The doping - temperature phase diagram of a hole doped cuprate. The green curve marks the pseudogap transition T^* . Solid line represents the (mean field) second order transition, while the dashed segment represent weakly first order one. The parabolic curve is the experimental superconductor - normal critical temperature in *Bi2212* measured in ref.¹⁸. Red points are T_c of our model, while the blue points are critical temperatures due to the apical phonon's pairing only (that is when the spin fluctuations are ignored).

In Appendix B the expressions for the electron correlators in both phases is given. The spectral weight namely the imaginary part of the symmetrized Green function, Eq.(B7), at zero frequency, exhibits the fractured Fermi surface qualitatively similar to ARPES observation^{47,55}.

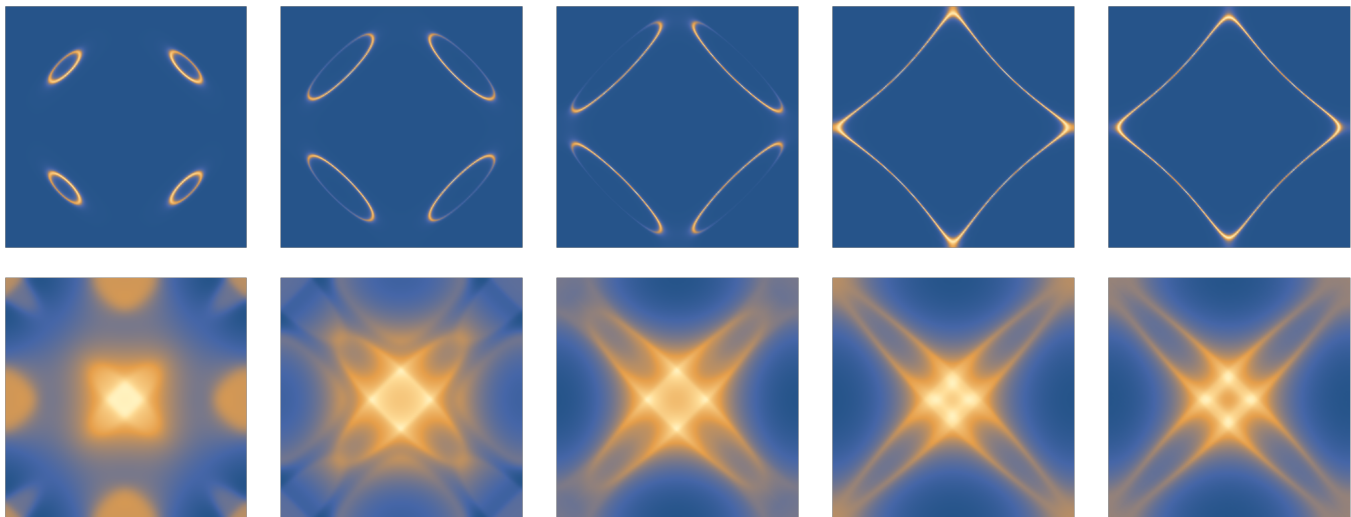


FIG. 4. Upper row: the quasi - particle spectral weight in nonsuperconducting ($x = 0.03$) underdoped ($x = 0.11, 0.15$), optimal doping ($x = 0.16$), and overdoped ($x = 0.18$) systems. Four Fermi arcs in underdoped case coalesce into a closed Fermi surface at the (Lifshitz) topological transition at optimal doping. Lower row: Spin susceptibility distribution of (in meV^{-1}) for the same doping levels. The distribution is continuous through the Lifshitz transition at optimal doping. Note that Brillouin zone in the upper row is centered at the crystallographic Γ point, while in the lower row it is shifted to the M point. This allows a convenient focus on the peak around the AF order $\mathbf{Q} = (\pi/a, \pi/a)$ point.

The spectral weigh for five values of doping are shown in the upper row in Fig.4. Two are in the non -superconducting state, $x = 0.02, 0.05$, one in the underdoped region, $x = 0.13$, optimal, $x = x^{opt} = 0.16$, and overdoped $x = 0.2$ regions. One observes that as the doping increases the length of the four Fermi arcs increases until the topological (Lifshitz) transition to a single Fermi surface at x^{opt} . Upon further hole doping the area of the enclosed region of BZ decreases. Note that the Fermi surface does not extend to the BZ boundary as seen in early experiments⁴³, however more recent measurements⁴⁷ apparently are consistent with this picture.

B. Phonon renormalization of the quasi - particle self energy and coupling constant λ^{ph}

1. Self energy due to phonons.

The quasiparticle (HF) self - energy is renormalized due to interaction with phonons. It generally leads to characteristic features of the spectrum like satellite bands¹⁴⁸, kinks in dispersion relation²⁸³⁰, etc. at energies of the order of the phonon frequency Ω above and below Fermi level. In our case (for details see a more general case considered in ref.¹⁷ and references therein) the Matsubara self energy for $x > x^{opt}$ (and temperature above T_c) in (gaussian or

renormalized) perturbation theory is:

$$\Sigma_{n\mathbf{k}} = \frac{(2\pi Z e^2)^2 T}{MN^2} \sum_{\mathbf{l}, m} \frac{e^{-2ld_a}}{\omega_m^{b2} + \Omega^2} \frac{1}{i\omega_{n+m} - E_{\mathbf{k}+1}}, \quad (11)$$

where

$$E_{\mathbf{p}} \equiv \epsilon_{\mathbf{p}} + \epsilon'_{\mathbf{p}} - \mu + Un/2. \quad (12)$$

The dispersion relations are given in Eq.(5) and M is the oxygen ion mass. Second order "gaussian" perturbation theory⁶² is justified at weak coupling, so that it should be confirmed in the following subsection that the dimensionless effective electron - electron coupling λ_{ph} is indeed small. Summing over the bosonic Matsubara frequencies, $\omega_m^{b2} = 2\pi Tm$, one obtains (after analytic continuation to physical frequency),

$$\begin{aligned} \Sigma(\omega, \mathbf{k}) &= \frac{(2\pi Z e^2)^2}{2M\Omega N^2} \sum_{\mathbf{l}} e^{-2d_a l} I_{\omega, \mathbf{k}+1}; \\ I_{\omega \mathbf{p}} &= \frac{f_B[\Omega] - f_F[-E_{\mathbf{p}}] + 1}{\omega + i\eta + \Omega - E_{\mathbf{p}}} + \frac{f_B[\Omega] + f_F[-E_{\mathbf{p}}]}{\omega + i\eta - \Omega - E_{\mathbf{p}}}, \end{aligned} \quad (13)$$

where $f_B[\varepsilon] = (\exp[\varepsilon/T] - 1)^{-1}$ is the Bose distribution.

In the underdoped case ($x < x^*$) we make use of the symmetrized correlators of the previous Subsection. The symmetrization is justified for description of the ARPES data, since it is a nonlocal probe, presumably over areas larger than the AF domain size. The results are similar in form to the underdoped case:

$$I_{\omega, \mathbf{k}} = Z_{\mathbf{k}}^+ \left(\frac{f_B[\Omega] - f_F[-E_{\mathbf{k}}^+] + 1}{\omega + i\eta + \Omega - E_{\mathbf{k}}^+} + \frac{f_B[\Omega] + f_F[-E_{\mathbf{k}}^+]}{\omega + i\eta - \Omega - E_{\mathbf{k}}^+} \right) + \{Z^+, E^+ \rightarrow Z^-, E^-\}. \quad (14)$$

Here energies $E_{\mathbf{k}}^{\pm}$ and weights $Z_{\mathbf{k}}^{\pm}$ are given in Eqs.(B9,B10). These expressions will be used for calculation of both the electron phonon coupling constant and the dispersion relation of quasi - particles.

2. Dimensionless electron - electron coupling λ

Generally the dimensionless coupling constant is defined in terms of the self energy as $\lambda_{\mathbf{k}} = -\frac{d}{d\omega} \Sigma(\omega, \mathbf{k})|_{\omega=0^+}$. In the overdoped case (see Appendix B for details and expressions in a more cumbersome underdoped case) one obtains at zero temperature:

$$\lambda_{\mathbf{k}} = \frac{2(\pi Z e^2)^2}{M\Omega N^2} \sum_{\mathbf{l}} e^{-2d_a l} \left\{ \frac{\theta[-E_{\mathbf{k}+1}]}{(E_{\mathbf{k}+1} - \Omega)^2} + \frac{\theta[E_{\mathbf{k}+1}]}{(E_{\mathbf{k}+1} + \Omega)^2} \right\}. \quad (15)$$

Results of numerical computation at the nodal point on the Fermi surface in the doping range from $x = 0.08$ to $x = 0.28$ is performed. At each doping the location of the Fermi surface point was given by an analytic solution. As expected it has a maximum of $\lambda^{ph} = 0.62$. Upon deviation from the angle 45° the coupling decreases. This is consistent with the experimental value estimated recently⁵⁶⁵⁷ at $30K$ to be $\lambda^{ph} = 0.41$ at optimal doping at $\mathbf{k} = (0, \pi)$. In the underdoped cases it vanishes at small angles due to finite extent of the Fermi arc, Generally the averaged over the Fermi surface coupling constant belongs to an intermediate range⁴⁰. Such coupling is sufficient (as will be shown also in the next Section) to provide high d-wave superconductivity $T_c \sim 80 - 90K$ at optimal doping, yet does not require the use of a rather problematic strong coupling Eliashberg theory. The coupling constitutes the bulk of the mechanism of superconductivity in the present paper (in addition to phonons the spin fluctuations also contribute to the overall effective coupling λ , see below).

The EPI renormalizes the quasiparticle spectrum and dynamics leading to several observations of the isotope substitution effect on the normal state properties. One of them is the "kink" in dispersion relation.

C. The "kink" function and the effect of the isotope substitution

It was established by ARPES early on that the hole dispersion relation abruptly changes derivative ("kink") in normal state approximately $45meV$ below Fermi level²⁸⁻³⁰. Although some other theories appeared, the large isotope

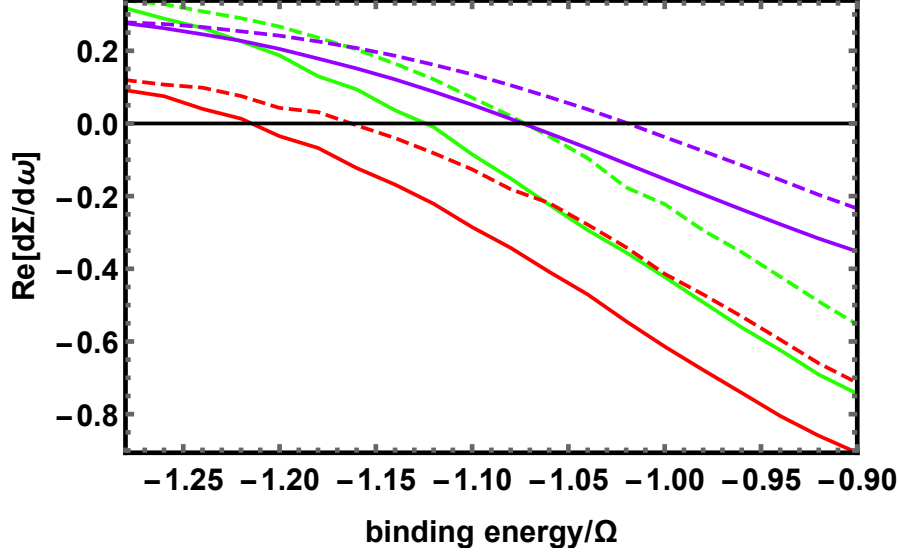


FIG. 5. Derivative of the self energy with respect to frequency at energies around Ω below the Fermi level. The values of doping are $x=0.13$ (green), $x=0.15$ (red) and $x=0.17$ (violet). The dash lines demonstrate isotope effect when ^{16}O is replaced by ^{18}O isotope. The kink appears when the derivative vanishes (blue line).

effect³¹ (substitution of ^{16}O isotope by ^{18}O), observed mainly in underdoped samples) provides evidence that the kinks should be attributed to EPI. To determine the kink position observed directly, let us differentiate the self energy Eq.(13) with respect to frequency ω . The real part of the integrand is:

$$\frac{d}{d\omega} I_{\omega, \mathbf{p}} = -\frac{f_B[\Omega] - f_F[-E_{\mathbf{p}}] + 1}{(\omega + i\eta + \Omega - E_{\mathbf{p}})^2} - \frac{f_B[\Omega] + f_F[-E_{\mathbf{p}}]}{(\omega + i\eta - \Omega - E_{\mathbf{p}})^2}, \quad (16)$$

where $E_{\mathbf{p}}$ was defined in Eq.(12). In the underdoped regime the expression is given in Appendix B.

To characterize the kink in dispersion relation, we calculate the derivative in range of frequencies between -1.3Ω to -0.9Ω for three dopings, 0.13 (green), 0.15 (red) and 0.17 (violet) in Fig.5. The kink position (zero value of the derivative) is around $\omega = -\Omega = -45\text{meV}$. The dashed lines are the same quantity but for a heavier isotope ^{18}O , namely with the oxygen atom mass M replaced by αM , $\alpha = 18/16$. The location is shifted by approximately 6%, as was indicated in the ARPES experiment²⁹. Now we turn to the main objective of the present study: d - wave superconductivity.

IV. SUPERCONDUCTIVITY.

Although the main emphasis of the paper is on the ALLP mechanism of the d - wave superconductivity in the hole doped cuprates, in the present Section we take into account also the magnetic fluctuation contribution. The reason is that the AF fluctuations were widely observed and in certain cases were shown to at least enhance superconductivity. The purpose of the present Section is to quantitatively compare the role of these two contributions and show how they coexist (complement each other) in the d - wave superconducting state. We start from the derivation of the phonon exchange d wave "potential" (mainly near the Γ point of BZ) and then proceed to the spin fluctuation one (mainly near the M point of the BZ).

A. Effective phonon and the spin fluctuation generated electron - electron interactions in spin singlet channel

In order to describe superconductivity, one should "integrate out" the phonon and the spin fluctuations degrees of freedom to calculate the effective electron - electron interaction. We start with the phonons. The Matsubara action for EPI, Eq.(8), and phonons, Eq.(3), are,

$$\frac{1}{T} \sum_{m,\mathbf{q}} \left(Z e^2 n_{-m,-\mathbf{q}} g_{\mathbf{q}}^{\alpha} u_{m,\mathbf{q}}^{\alpha} + \frac{M}{2} u_{-m,-\mathbf{q}}^{\alpha} \Pi_{m,\mathbf{q}}^{\alpha\beta} u_{m,\mathbf{q}}^{\beta} \right), \quad (17)$$

where $n_{-n,-\mathbf{q}} = \sum_{\mathbf{k},m} \psi_{\mathbf{k}-\mathbf{q},m-n}^{*\sigma} \psi_{\mathbf{k},m}^{\sigma}$ and g was defined in Eq.(9). The polarization matrix is defined via the dynamic matrix of Eq.(3): $\Pi_{n,\mathbf{q}}^{\alpha\beta} = (\omega_n^b)^2 \delta_{\alpha\beta} + M^{-1} D_{\mathbf{q}}^{\alpha\beta}$, $\alpha, \beta = x, y$, calculated in Appendix A. Since the action is quadratic in the phonon field \mathbf{u} , the partition function is gaussian and can be integrated out exactly, see details in ref.¹⁷. As a result one obtains the effective density - density interaction term for of electrons

$$A_{eff}^{ph} = \frac{1}{2T} \sum_{\mathbf{q},n} n_{n,\mathbf{q}} v_{n\mathbf{q}}^{ph} n_{-n,-\mathbf{q}}; \quad v_{n,\mathbf{q}}^{ph} = -\frac{(2\pi Z e^2)^2 e^{-2d_a|\mathbf{q}|}}{M \omega_n^{b2} + \Omega^2}. \quad (18)$$

The expression is "exact" for harmonic phonons (we have neglected the transversal mode and small dispersion of the longitudinal mode spectrum¹⁷, see Fig. 2). An approximate expression for the effective interaction due to the electron correlations effects will be derived next. The potential exhibits the central "inverted" (that is negative) "peak" that we will call the apical phonon dip due to the exponential form of the matrix element. The second bosonic "glue" is generated by the correlation effects.

Since, as explained in Subsection IIIA, the renormalized on site repulsion constant in our scheme, \bar{U} is not very large (see Table III), the gaussian expansion^{39,58} is applicable. One starts with the mean field GF and considers the rest of the action as a perturbation. In the overdoped case, it is just a "renormalized" Kohn-Luttinger perturbation theory⁵⁹. We therefore calculate the effective interaction due to correlations in the second order in U_r . Generally, utilizing the inversion symmetry, the effective interaction in the spin singlet channel has a form:

$$A_{eff}^{cor} = \frac{1}{2T} \sum_{\mathbf{q},n} n_{n\mathbf{q}} v_{n\mathbf{q}}^{cor} n_{-n,-\mathbf{q}}; \quad v_{m\mathbf{q}}^{cor} = U_r + U_r^2 \chi_{m\mathbf{q}}, \quad (19)$$

where $\chi_{m\mathbf{q}}$ is the electronic susceptibility. The positive constant U_r in Eq.(19) is just the direct first order Coulomb repulsion suppressing the s-wave pairing, but having no impact on the d - wave pairing.

The well known Kohn-Luttinger diagrams^{38,59} give in the overdoped case, $x > x^*$, the following dynamic Matsubara susceptibility:

$$\chi_{m\mathbf{q}} = \frac{1}{N^2} \sum_{\mathbf{p}} \frac{f_F[E_{\mathbf{p}+\mathbf{q}}] - f_F[E_{\mathbf{p}}]}{i\omega_m + E_{\mathbf{p}} - E_{\mathbf{p}+\mathbf{q}}}, \quad (20)$$

where $E_{\mathbf{p}}$ was defined in Eq.(12). This is calculated numerically for sufficiently large values of $N = 256$ and harmonics $|m| \leq 32$. In the lower row of Fig.5 the static part, namely zero frequency is given $x = x^{opt} = 0.16$ and $x = 0.2$. Similarly in the underdoped case, $x < x^*$, one calculates the same two diagrams on the magnetic BZ, $0 < k_1 < \pi$, $-\pi < k_2 < \pi$, namely using the GF of Eq.(B7). Since we are interested in the dynamic susceptibility on the scale of the Cooper pairs, the full sublattice matrix should be used. This is derived in Appendix B, where a rather bulky expression, Eq.(B13) is given. It turns out that after symmetrization it is not much different from the overdoped case susceptibility as is shown in Fig. 5. The symmetrization of the susceptibility matrix is made as in ref.³⁹). The zero frequency χ_{0,k_x,k_y}^{sym} at $T = 50K$ is plotted for $x = 0.13$. The dependence on temperature in the relevant range ($T < 300K$) is very weak. One observes that the evolution is smooth through the Lifshitz point x^{opt} .

The general feature of the Matsubara susceptibility distribution over the BZ is that near the crystallographic M point the susceptibility is large, while near the Γ point it is small. This is crucial for the d - wave pairing. Note also the fine structure of the susceptibility: there are two characteristic local maxima near point M , while the point itself is a local minimum. The splitting is very small. In this paper we do not consider possible fourfold symmetry breaking (or nematicity). This effective electron - electron couplings will be used in the gap equation.

B. Superconducting gap

To complete the electronic effective action, one adds to Eqs.(18) and (19) the electronic part,

$$\mathcal{A}_{eff} = \frac{1}{T} \sum_{\mathbf{n}\mathbf{k}} \left\{ \psi_{\mathbf{n}\mathbf{k}}^{*\sigma} G_{\mathbf{n}\mathbf{k}}^{-1} \psi_{\mathbf{n}\mathbf{k}}^{\sigma} + \frac{1}{2} n_{\mathbf{n}\mathbf{k}} v_{\mathbf{n}\mathbf{k}} n_{-\mathbf{n}, -\mathbf{k}} \right\}; \quad (21)$$

where $v_{\mathbf{n}\mathbf{q}} = v_{\mathbf{n}\mathbf{q}}^{ph} + v_{\mathbf{n}\mathbf{q}}^{cor}$, G is the (HF) Green's function and v^{ph} and v^{cor} are given by Eq.(18) and Eq.(19) respectively. The standard superconducting gap equation is,

$$\Delta_{m\mathbf{k}} = -\frac{T}{N^2} \sum_{n\mathbf{p}} \frac{v_{m-n, \mathbf{k}-\mathbf{p}}}{G_{n\mathbf{p}}^{-1*} \Delta_{n\mathbf{p}}^{-1} G_{n\mathbf{p}}^{-1} + \Delta_{n\mathbf{p}}^*}. \quad (22)$$

Here the (Matsubara) gap function is related to the anomalous GF, $\langle \psi_{m\mathbf{k}}^{\sigma} \psi_{n\mathbf{p}}^{\rho} \rangle = \delta_{n+m} \delta_{\mathbf{k}+\mathbf{p}} \varepsilon^{\sigma\rho} F_{m\mathbf{k}}$ ($\varepsilon^{\sigma\rho}$ - the anti-symmetric tensor), by

$$\Delta_{m\mathbf{k}} = \frac{T}{N^2} \sum_{n\mathbf{p}} v_{m-n, \mathbf{k}-\mathbf{p}} F_{n, \mathbf{p}}. \quad (23)$$

The gap equation was solved numerically by iteration for $N = 256$ and 64 frequencies. It converges to the d - wave solution. An example of the gap distribution over the BZ (for the optimal doping at $T = 50K$) is given in figure in Appendix C. The absolute value of the Matsubara gap function has a maximum near the crystallographic X point $(0, \pi)$. This value as function of doping and temperature is given in figure in Appendix C.

In an AF domain (considered to be larger than the Cooper pair) the fourfold symmetry is broken. As a consequence one uses basis consisting of two sublattices $I = A, B$ and the magnetic BZ defined in Appendix B. The electronic effective action, in this basis takes a form

$$\mathcal{A}_{eff} = \frac{1}{T} \sum_{\mathbf{n}\mathbf{k}} \left\{ \psi_{\mathbf{n}\mathbf{k}}^{*\sigma I} [G_{\mathbf{n}\mathbf{k}}^{-1\sigma}]^{IJ} \psi_{\mathbf{n}\mathbf{k}}^{\sigma J} + \frac{1}{2} n_{\mathbf{n}\mathbf{k}}^{\sigma I} v_{\mathbf{n}\mathbf{k}}^{\sigma\rho IJ} n_{-\mathbf{n}, -\mathbf{k}}^{\rho J} \right\}, \quad (24)$$

where G is the (HF) Green's function is given in Eq.(B7) in Appendix B. The symmetrized susceptibility in the underdoped cases of $x = 0.02, 0.05, 0.13$ are given in Fig.5. One observes that the distribution is continuously crosses over to the overdoped one via the (Lifshitz) topological transition at optical doping.

The anomalous Green's function is also a 2×2 matrix in sublattice space. For singlet pairing one has: $\langle \psi_{n, \mathbf{k}}^{\sigma I} \psi_{-n, -\mathbf{k}}^{\rho J} \rangle = \varepsilon^{\sigma\rho} F_{n\mathbf{k}}^{IJ}$. Assuming the up-down (singlet) pairing¹⁷, see Appendix C,

$$[\Delta_{n\mathbf{k}}] = \begin{pmatrix} 0 & \Delta_{n\mathbf{k}}^{\uparrow\downarrow} \\ \Delta_{n\mathbf{k}}^{\downarrow\uparrow} & 0 \end{pmatrix}; \quad \Delta_{n\mathbf{k}}^{\uparrow\downarrow IJ} = \sum_{m\mathbf{p}} v_{n-m, \mathbf{k}-\mathbf{p}}^{\uparrow\downarrow IJ} F^{\uparrow\downarrow IJ}, \quad (25)$$

the gap equation in matrix form becomes,

$$[\Delta_{n\mathbf{k}}^{\uparrow\downarrow}] = -\sum_{m\mathbf{p}} [v_{n-m, \mathbf{k}-\mathbf{p}}] * \left\{ [G_{m\mathbf{p}}^{-1\downarrow}]^{\dagger} [\Delta_{m\mathbf{p}}^{\uparrow\downarrow}]^{-1} [G_{m\mathbf{p}}^{-1\uparrow}] + [\Delta_{m\mathbf{p}}^{\uparrow\downarrow}]^{\dagger} \right\}^{-1}, \quad (26)$$

and the same for $\Delta_{n\mathbf{k}}^{\downarrow\uparrow}$. The star product denotes the matrix element multiplication. The iteration solution for the same system size, as in the overdoped case, converges to the d - wave solution for wide range of initial conditions. The results for various temperatures are given in SM C, while critical temperatures with (without) spin fluctuations are presented as black (green) point in Fig.4. In the concluding section the results are qualitatively discussed.

The line of vanishing gap determines the T_c values on the phase diagram in Fig.4 (red squares). In the underdoped domain it comes short of the parabolic experimental dependence¹⁸ (dashed curve). If one neglects the magnon contribution, namely takes $v = v^{ph}$, the temperatures are lower by 15-20% (red circles).

C. Isotope effect

The influence of the oxygen isotope substitution, $^{16}O \rightarrow ^{18}O$ on superconductivity can be gauged by calculation of the change of the (Matsubara) gap at a temperature below T_c . In Fig.6 we plot the The deduced exponent,

$$\alpha = \frac{18}{16} \log \frac{\Delta(^{16}O)}{\Delta(^{18}O)}, \quad (27)$$

at temperature $T = 20K$.

The same exponent was estimated by measuring the T_c isotope effect in various hole doped cuprates⁶⁰, mostly in $YBa_2Cu_3O_{7-x}$ and $La_{2-x}Sr_xCuO_4$. Qualitatively the exponent is small in overdoped and optimally doped materials, but increases at strongly overdoped case. In $Ba_2Sr_2CaCu_2O_7$ the experimental results are scarce, but order of magnitude is the same as in Fig. 6.

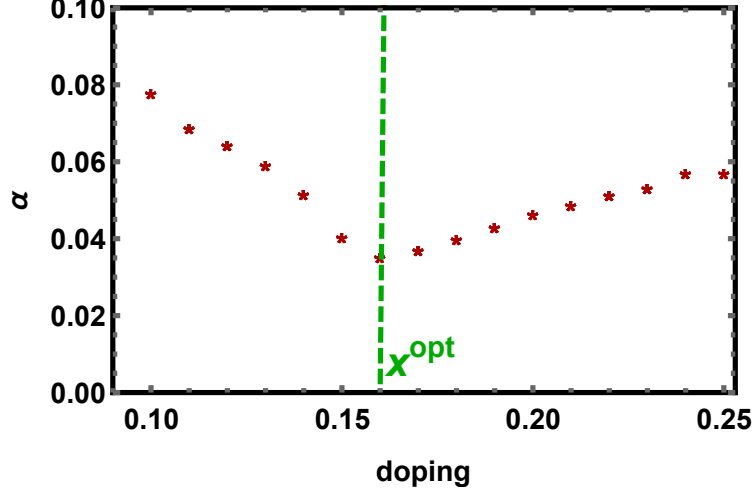


FIG. 6. Isotopic effect critical exponent versus doping

The isotope effect exponential is small, at optimal and overdoped systems, however it slightly increases when the doping is reduced below optimal (reaches $\alpha = 0.08$ at $x = 0.1$).

D. Thermal fluctuations and the inter-layer tunneling

In the bi-layer *Bi2212* there are two types of tunneling. The first is a rather strong tunneling between adjacent layers within the bi-layer is estimated⁴³ to be $t'_\perp = 30 - 80meV$. It leads to appearance of the secondary band mentioned in Section II. The second tunneling amplitude is between the bi-layers in different cells. The 3D dispersion relation is $\epsilon_{\mathbf{k},k_z} = \epsilon_{\mathbf{k}} + \epsilon'_{\mathbf{k}} + t_\perp \cos(k_z s)$, where $\epsilon_{\mathbf{k}}, \epsilon'_{\mathbf{k}}$ are given in Eq. (4) and s - the inter bi-layers separation. The order of magnitude is much smaller than t'_\perp : $t_\perp = 1 - 2meV$.

Superconductivity in a single *CuO* bi-layer is of the 2D Kosterlitz -Thouless type. The mean field critical temperature calculated above slightly overestimates T_{KT} , where the modulus of the order parameter is established: $T_c - T_{KT} \approx T_c Gi_{2D}$. Here Gi_{2D} is the 2D Ginzburg number, $Gi_{2D} = a^2/d\xi_\parallel$, d is the thickness of the *CuO* bi-layer and ξ_\parallel is the lateral coherence length⁶². Due to the tunnelings t_\perp between bi - layers makes the system 3D and the KT feature disappears.

The 2D/3D crossover occurs when $\xi_\perp \sim s$ where ξ_\perp are the coherence length in z - direction. Close to the critical temperature $\xi_\perp \sim \hbar v_z/T_c \sqrt{1 - T/T_c}$, where $\hbar v_z = \frac{\partial \epsilon}{\partial k_z} = t_\perp s$. It determines the temperature range in which the superconductivity is essentially 3D: $|1 - T/T_c| < (t_\perp/T_c)^2 \sim 0.02$.

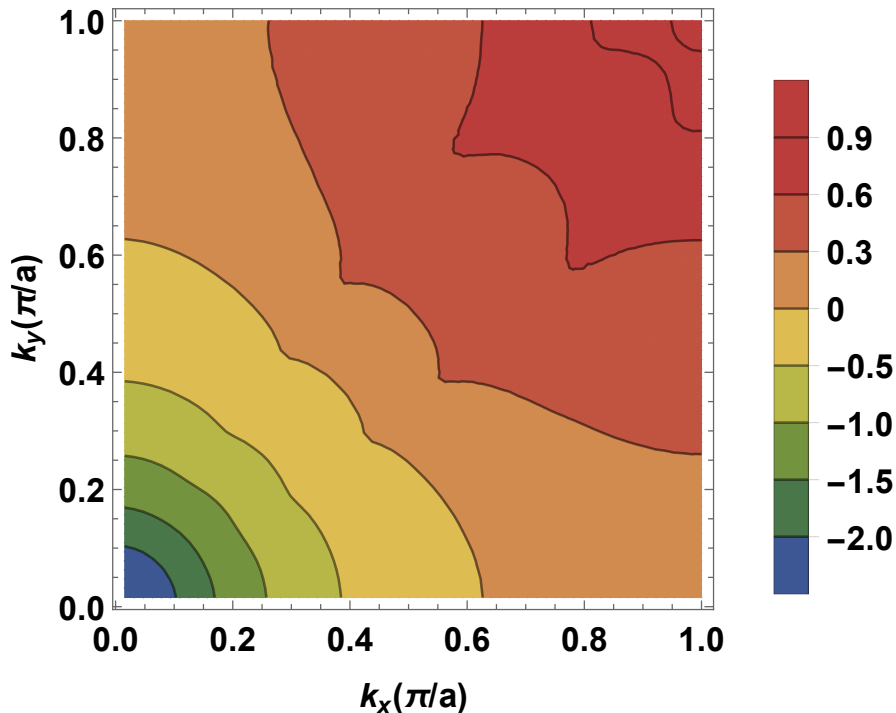


FIG. 7. The overall potential including both the phonon central dip at Γ and the correlation peak at M . Note that the dip is larger than the peak leading to dominance of the phonon channel.

V. DISCUSSION AND CONCLUSIONS.

A. Summary

Theory of superconductivity of high T_c cuprates based on the dominant ALLP pairing mechanism was proposed. It is comprehensive in a sense that the whole doping range is considered including anomalous normal state properties of cuprates like $Bi_2Sr_2CaCu_2O_{8+x}$. To demonstrate the basic principles we limited ourselves in this paper to a simple sufficiently generic model: the pseudogap physics of 2DEG in the CuO planes is described by the fourfold symmetric $t-t'$ single band Hubbard model with on site repulsion energy U of moderate strength. Doping is controlled by the chemical potential.

The results are following. The most important for the pairing mode for $Bi2212$ is found to be the optical longitudinal lateral (within the SrO plane) mode at $45meV$, mostly due to vibration of apical oxygen atoms. The dimensionless electron - electron attraction exhibits an exponential forward scattering peak and is estimated to have the strength of $\lambda \sim 0.6$. When parameters of the effective one band $t-t'$ model of 2DEG were fixed at $t' \sim -0.17t$ and $U \sim 6t$, $t = 0.3eV$, the mean field T^* line, green curve in phase diagram, fig.3, become a crossover between short range AF pseudogap phase and the paramagnetic one. The quasi - particle spectrum undergoes a topological (Lifshitz) transition. The closed Fermi surface above the T^* line disintegrates into four Fermi arcs below it, see Fig. 4.

Renormalization of the electron Green's function due to phonons allows calculation of the quasi - particle properties. Location of kink in dispersion relation including the observed isotope ($^{16}O \rightarrow ^{18}O$) dependence, see Fig. 5. Since the electron - phonon coupling λ is moderate, weak coupling dynamic Eliashberg approach is applicable to calculate the gap function and critical temperature T_c . One has to go beyond the BCS approximation due to important dependence

of the phonon mediated pairing on frequency. Both phonon and spin fluctuation pairing are accounted for over the full doping range. It is found that the critical temperatures above $90K$ at optimal doping can be reached, see Fig. 4. The dominant "glue" responsible for the d - wave pairing turns out to be the phonon mode rather than spin fluctuations, although the later enhances superconductivity by about 15-20%. Comparison of the doping dependence of T_c with experimental¹⁸ is qualitatively fair, although . underdoped are slightly underestimated, while strongly overdoped overestimated. The isotope ($^{16}O \rightarrow ^{18}O$ substitution) effect is small at optimal doping but increases towards both the underdoped and the overdoped regions, see Fig.6. This is consistent with observations³¹.

B. Qualitative picture of the d-wave superconductivity

Let us now make an argument qualitatively describing the d - wave pairing by ALLP and its coexistence with spin fluctuations or other pairing "glue". Generally the pairing potential v should have sufficiently large dependence on momentum over BZ. The overall pairing potential, Eq.(21) is a sum of the phonon and the spin fluctuations contributions. The ALLP's forward scattering peak presents itself as a large dip of the potential at the Γ point, see Fig. 7, due to attractive nature of the EPI. In contrast the spin susceptibility peak of Fig. 4 causes a smaller maximum B5 at the M point (corner of Brillouin zone), since the interaction is repulsive. Both regions of the BZ contribute to d-wave superconductivity and fortunately do not interfere with each other. Indeed the phonon peak decreases exponentially to just 10% at distance $k^{ph} = \frac{1}{d_a} = \frac{2\pi}{3a}$, where d_a is the vertical distance of the CuO layer from the SrO layer, see Fig. 1. The susceptibility becomes negligible at distance $\frac{\pi}{3a}$ from M , see Fig.4. Hence the BZ is effectively utilized.

To summarize, two features turned out to be sufficient for robust apical phonon d - wave pairing. The first is the rhombic shape of the Fermi surface. The second is the exponential FSP of the apical lateral phonon optical mode and, to a lesser degree, constructive cooperation with the spin fluctuation channel. The s-wave solution of the gap equation sometimes competes with the d - wave that appears only when the fourfold anisotropy of the Fermi surface is sufficiently pronounced. In these cases the central peak favors d-wave over the s-wave due to two reasons. First, the s-wave pairing due to the apical phonons is generally weaker than the CuO plane phonons since unlike in BCS large momentum q contributions are suppressed. Second, while the s-wave channel is suppressed by direct Coulomb repulsion, the d-wave *is not* (the quasi - local Coulomb repulsion drops out of the gap equation for the d-wave). We have explicitly compared energies and found that the s-wave loses in the range presented.

C. Concluding remarks

Restriction of the description of the electron gas to one band Hubbard model with just two parameters t, t' for nearest neighbor and next to nearest neighbor hopping obviously makes the model less realistic to quantitatively describe real materials like $Bi2212$. These typically require either a three band much more complicated model or an effective one band model with more distant hopping terms like t'' . In addition the tunneling between the conducting CuO planes via a metallic layer and the nematicity (deviations from the fourfold symmetry) should be added. These lead to a characteristic splitting of the spectrum⁴³. This is left for future work. Of course the phenomena broadly termed "unusual normal and superconducting properties of high T_c cuprates" contains many more features. In this paper we have emphasized ones that are directly linked to the phonon exchange.

Experimentally the main claim of the paper, namely that the "glue" that creates d - wave pairing is the phonon exchange of a very specific nature, the apical oxygen's (that is one belonging to an insulating layer, SrO , adjacent to the conducting CuO layer) lateral vibrations, can be further directly strengthened or falsified by suppression such vibrations as in refs²⁵²⁷ or actively focus on these modes and their coupling. Since one or two unit cell perovskite were recently fabricated²⁰¹⁸¹⁹ perhaps apical oxygen atoms can be distinguished from the rest. An alternative route is to look for secondary effects of this coupling on normal state properties, some calculated in the present paper. The phonons induce modifications in normal state like modification of dispersion relation on transport beyond the "strange metal" resistivity behavior. The modification can be isolated by isotope substitution. Superconducting properties due to this particular mechanisms in addition to T_c and order parameter studied, are also sensitive to the isotope substitution. An example is magnetization curves⁶¹ that simply depend on T_c (via Ginzburg - Landau description⁶²).

Acknowledgements.

We are grateful Prof. D. Li, H.C. Kao, T. X. Ma, L. L.Wang, Y. Guo, J.Y. Lin and Y. Yeshurun for helpful discussions. Work of B.R. was supported by NSC of R.O.C. Grants No. 101-2112-M-009-014-MY3.

Appendix A: A. The apical oxygen lateral vibration modes and their coupling to holes in the CuO plane.

1. The apical oxygen lateral branches

The approximate method of determining the relevant vibration modes is the same as previously used for the *FeSe* on STO superconductor, see details in Appendix A of ref.¹⁷. The chart on the right in Fig. A1 is a view from above with sphere radii corresponding to the repulsive Born - Meyer potential ranges given in Table I. Unit cell including both the metallic layer and the substrate is marked by the black frame in Fig. 8. Dynamic degrees of freedom are the *O* atoms in the *SrO* layer, see Fig.8.

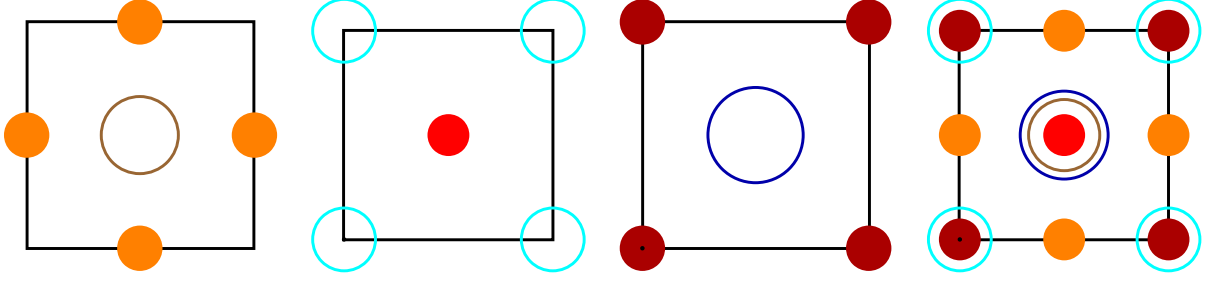


FIG. 8. Atomic lateral positions of the three layers a. the 2DEG layer consisting of *Cu* at $\mathbf{R}^{Cu} = (0, 0, z^{Cu})$ and two O_1 atoms at $\mathbf{R}^{Ox} = (a, a/2, z^{Cu})$ and $\mathbf{R}^{Oy} = (a/2, a, z^{Cu})$. b. the apical phonon layer containing the *Sr* at origin $\mathbf{R}^{Sr} = (0, 0, 0)$ and $\mathbf{R}^{Oy} = (a/2, a, z^{Cu})$ and O_2 at $\mathbf{R} = (a/2, a/2, 0)$. c. the third layer: *Bi* at $\mathbf{R}^{Bi} = (a/2, a/2, z^{Bi})$ and O_3 at $\mathbf{R}^{O3} = (0, 0, z^{Bi})$. d. The top view: all the three layer's projections are superimposed.

Hamiltonian for these degrees of freedom is:

$$H_{ph} = K_{ph} + W. \quad (\text{A1})$$

Here kinetic energy is

$$K_{ph} = \frac{M}{2} \sum_{\mathbf{n}} \left(\frac{d}{dt} \mathbf{u}_{\mathbf{n}} \right)^2, \quad (\text{A2})$$

while the potential energy part W consists of interatomic Born - Meyer potentials defined in Eq.(2). Only interactions of the "dynamic" oxygen atoms in the *SrO* with neighboring *BiO* below and *CuO* above are taken into account:

$$W = \frac{1}{2} \sum_{\mathbf{n}, \mathbf{m}} \left\{ \begin{array}{l} v^{SrO} [\mathbf{R}^{Sr} + \mathbf{r}_{\mathbf{n}} - \mathbf{r}_{\mathbf{m}} - \mathbf{u}_{\mathbf{m}}] + v^{CuO} [\mathbf{R}^{Cu} + \mathbf{r}_{\mathbf{n}} - \mathbf{r}_{\mathbf{m}} - \mathbf{u}_{\mathbf{m}}] \\ + v^{OO} [\mathbf{R}^{Ox} + \mathbf{r}_{\mathbf{n}} - \mathbf{r}_{\mathbf{m}} - \mathbf{u}_{\mathbf{m}}] + v^{OO} [\mathbf{R}^{Oy} + \mathbf{r}_{\mathbf{n}} - \mathbf{r}_{\mathbf{m}} - \mathbf{u}_{\mathbf{m}}] \\ + v^{BiO} [\mathbf{R}^{Bi} + \mathbf{r}_{\mathbf{n}} - \mathbf{r}_{\mathbf{m}} - \mathbf{u}_{\mathbf{m}}] + v^{OO} [\mathbf{R}^{O3} + \mathbf{r}_{\mathbf{n}} - \mathbf{r}_{\mathbf{m}} - \mathbf{u}_{\mathbf{m}}] \end{array} \right\} + \frac{1}{2} \sum_{\mathbf{n} \neq \mathbf{m}} v^{OO} [\mathbf{r}_{\mathbf{n}} - \mathbf{r}_{\mathbf{m}} + \mathbf{u}_{\mathbf{n}} - \mathbf{u}_{\mathbf{m}}]. \quad (\text{A3})$$

Here the lateral apical oxygen positions are

$$\mathbf{r}_{\mathbf{m}} = a (m_1, m_2), \quad (\text{A4})$$

while positions of the heavy *Sr, Cu, Bi*, see Figs. 8, are

$$\begin{aligned} \mathbf{R}^{Sr} &= a \left(\frac{1}{2}, \frac{1}{2}, 0 \right); \\ \mathbf{R}^{Cu} &= z_{Cu} \hat{\mathbf{z}}; \\ \mathbf{R}^{Bi} &= z_{Bi} \hat{\mathbf{z}}. \end{aligned} \quad (\text{A5})$$

The inter-layer spacings are given in Table I and $\hat{\mathbf{z}} \equiv (0, 0, 1)$. The positions of the two oxygen atoms of the CuO_2 layer and that in the BiO layer are:

$$\mathbf{R}^{Ox} = (0, a/2, z_{Cu}); \quad \mathbf{R}^{Oy} = (a/2, 0, z_{Cu}); \quad \mathbf{R}^{O3} = (0, 0, z_{Bi}). \quad (\text{A6})$$

Consequently the dominant lateral displacements, $u_{\mathbf{m}}^\alpha$, $\alpha = x, y$, are of the apical oxygen atoms.

Vibrations of heavy atoms and even oxygen in other planes are not expected to be significant due to their mass or distance from the SrO layer oxygen atoms. Some effects of those vibrations can be accounted for by the effective oxygen mass, while more remote layers above and below the important layer were checked to be negligible.

Harmonic approximation consists of expansion around a stable minimum of the energy. Expressions for the derivatives are given in ref.¹⁷. This leads to the following expression for the dynamic matrix

$$\begin{aligned} D_{\mathbf{k}}^{\alpha\beta} = & \sum_{\mathbf{n}} [v^{CuO}]_{\alpha\beta}'' [\mathbf{R}^{Cu} + \mathbf{r}_{\mathbf{n}}] + [v^{OO}]_{\alpha\beta}'' [\mathbf{R}^{Ox} + \mathbf{r}_{\mathbf{n}}] \\ & + [v^{OO}]_{\alpha\beta}'' [\mathbf{R}^{Oy} + \mathbf{r}_{\mathbf{n}}] + [v^{SrO}]_{\alpha\beta}'' [\mathbf{R}^{Sr} + \mathbf{r}_{\mathbf{n}}] + [v^{BiO}]_{\alpha\beta}'' [\mathbf{R}^{Bi} + \mathbf{r}_{\mathbf{n}}] \\ & + [v^{BiO}]_{\alpha\beta}'' [\mathbf{R}^{O3} + \mathbf{r}_{\mathbf{n}}] + (1 - \exp[-i\mathbf{k} \cdot \mathbf{r}_{\mathbf{n}}]) [v^{OO}]_{\alpha\beta}'' [\mathbf{r}_{\mathbf{n}}]. \end{aligned} \quad (\text{A7})$$

These matrix elements determine the frequencies (eigenvalues) for the two polarizations presented in Fig. 2.

2. The electron - phonon matrix elements

The microscopic derivation of the electron - phonon coupling of the holes residing in the CuO plane should in principle start at least from an effective three band (Emery) model of cuprate⁶³. It is often reduced to the two band⁶⁴ model consisting of the Zhang - Rice singlet state, a symmetric combination of the (in plane) $2p_x$ and $2p_y$ O orbitals, and the $3d_{x^2-y^2}$ Cu orbitals. Let us assume a simplified picture case that the hole's wave function is concentrated on two oxygen positions within the unit cell. Concentrating on one unit cell, drawn in Fig. 8a (left) as a black square, the 2D density is:

$$|\varphi(\mathbf{r})|^2 = \frac{1}{4} \left\{ \begin{array}{l} \delta(\mathbf{r} + a(1/2, 0)) + \delta(\mathbf{r} - a(1/2, 0)) \\ + \delta(\mathbf{r} + a(0, 1/2)) + \delta(\mathbf{r} - a(0, -1/2)) \end{array} \right\}; \quad (\text{A8})$$

$$n_1(\mathbf{r}) = \frac{1}{N^2} |\varphi(\mathbf{r} - \mathbf{r}_1)|^2. \quad (\text{A9})$$

Extent of the density distribution in the z direction is neglected.

The electron - ion electrostatic energy is,

$$H_{ei} = -e \int_{\mathbf{r}} \Phi(\mathbf{r}) n(\mathbf{r}), \quad (\text{A10})$$

where the potential was given by Eq.(7) and the electron density (due to the localization of the wave functions independent of the electron quasi - momentum \mathbf{k} , see ref.⁶⁵), $n(\mathbf{r}) \propto \sum_{\mathbf{l}} n_1(\mathbf{r})$. Substituting and expanding to first order in the oxygen vibrations, one obtains:

$$H_{ei} = -Ze^2 \sum_{\mathbf{l}, \mathbf{m}} \int_{\mathbf{r}} \frac{(\mathbf{r} - \mathbf{r}_{\mathbf{m}}) \cdot \mathbf{u}_{\mathbf{m}}}{((\mathbf{r} - \mathbf{r}_{\mathbf{m}})^2 + d_a^2)^{3/2}} n_1(\mathbf{r}). \quad (\text{A11})$$

Fourier transforming u this takes a form:

$$H_{ei} = Ze^2 \sum_{\mathbf{q}} n_{-\mathbf{q}} g_{\mathbf{q}}^\alpha u_{\mathbf{q}}^\alpha, \quad (\text{A12})$$

where $n_{\mathbf{q}} = \int_{\mathbf{r}} e^{i\frac{2\pi}{N}\mathbf{q} \cdot \mathbf{r}} n_1(\mathbf{r})$ and with the matrix element

$$g_{\mathbf{q}}^\alpha = \frac{1}{2} \left(\cos \frac{aq_x}{2} + \cos \frac{aq_y}{2} \right) \bar{g}_{\mathbf{q}}^\alpha. \quad (\text{A13})$$

The "local" matrix element function,

$$\bar{g}_{\mathbf{q}}^{\alpha} = \sum_1 e^{i\frac{2\pi}{N}\mathbf{q}\cdot\mathbf{l}} \frac{\mathbf{r}_1^{\alpha}}{(\mathbf{r}_1^2 + d_a^2)^{3/2}}, \quad (\text{A14})$$

would be obtained if the hole is localized right above the apical oxygen. The summation in a very good approximation over the BZ can be replaced by integration with the result given in Eq.(9).

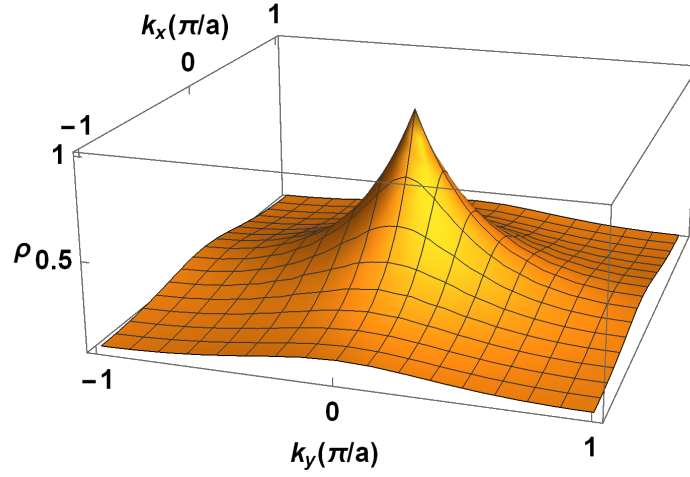


FIG. 9. Square of the matrix element of the electron - phonon coupling. Decreases exponentially as function of quasi - momentum momentum away from the Γ point. The forward scattering peak region occupies a significant portion of the Brillouin zone.

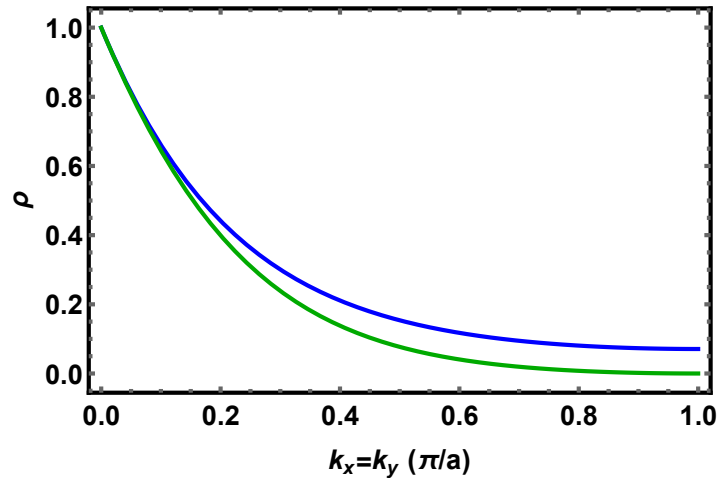


FIG. 10. Square of the matrix element of the electron - phonon coupling. Decreases exponentially as function of quasi - momentum momentum away from the Γ point. The forward scattering peak region occupies a significant portion of the Brillouin zone.

Appendix B: B. Normal state properties

1. Coupling renormalization and the effective HF in overdoped and underdoped regime.

The HF theory of the $t-t'$ model has been thoroughly investigated over the years⁶⁶⁶⁷. The spin rotation $SU(2)$ symmetry in anti-ferromagnet is broken down to its $U(1)$ subgroup. The on site magnetization, $M = \frac{1}{2}(n^{A\downarrow} - n^{A\uparrow}) = \frac{1}{2}(n^{B\uparrow} - n^{B\downarrow})$, is considered to be oriented along the spin space z axis. The lattice translation symmetry consequently is reduced to a smaller one on two sublattices $I = A, B$. The sublattice A consists of odd $(i_x + i_y)$ sites, while B contains even $(i_x + i_y)$ sites. Position within the sublattices can be specified by integers $i_1 = 1, \dots, N/2 \equiv N'$ and $i_2 = 1, \dots, N$, namely $c_{i_1, i_2}^A = c_{2i_1-1+i_2, i_2}$ and $c_{i_1, i_2}^B = c_{2i_1+i_2, i_2}$.

Hamiltonian in the magnetic quasi-momentum \mathbf{k} space becomes (integer momenta) is,

$$K = \sum_{k_1 k_2} \left\{ - \left(c_{\mathbf{k}}^{A\uparrow} h_{\mathbf{k}}^* a_{\mathbf{k}}^B + h.c. \right) + c_{\mathbf{k}}^{I\uparrow} (\varepsilon'_{\mathbf{k}} - \mu) c_{\mathbf{k}}^I \right\}, \quad (\text{B1})$$

where

$$\begin{aligned} h_{\mathbf{k}} &= t \left\{ 1 + \exp \left[\frac{2\pi i}{N} (2k_1 - k_2) \right] + \exp \left[\frac{2\pi i}{N'} k_1 \right] + \exp \left[\frac{2\pi i}{N} k_2 \right] \right\}; \\ \varepsilon'_{\mathbf{k}} &= -4t' \cos \left[\frac{2\pi}{N} k_1 \right] \cos \left[\frac{2\pi}{N} (k_1 - k_2) \right]. \end{aligned} \quad (\text{B2})$$

The HF equations takes a form (using $n^{A\uparrow} \equiv n_1, n^{A\downarrow} = n_2$ electron densities on each site, no charge density wave appear in the model considered),

$$n_1 = F[n_1, n_2]; \quad n_2 = F[n_2, n_1],$$

where the function F is defined by

$$F[n_1, n_2] = \frac{1}{NN'} \sum_{\mathbf{k}} \left\{ f_F[E_{\mathbf{k}}^-] - \frac{\Delta_{pg} + x_{\mathbf{k}}}{4x_{\mathbf{k}}} \left(\tanh \left[\frac{E_{\mathbf{k}}^+}{2T} \right] - \tanh \left[\frac{E_{\mathbf{k}}^-}{2T} \right] \right) \right\}. \quad (\text{B3})$$

Here $\Delta_{pg} \equiv U_r M$ is the pseudogap energy and $f_F(\varepsilon) \equiv (\exp[\varepsilon/T] + 1)^{-1}$ is the Fermi-Dirac distribution. The new quasi-particle (hole in our case) spectrum consists of two branches

$$E_{\mathbf{k}}^{\pm} = \varepsilon'_{\mathbf{k}} - \mu + U_r \frac{n_1 + n_2}{2} \pm x_{\mathbf{k}}. \quad (\text{B4})$$

and

$$x_{\mathbf{k}}^2 \equiv \Delta_{pg}^2 + |h_{\mathbf{k}}|^2. \quad (\text{B5})$$

The fact that the transition is second order is verified by the fitting of the pseudogap curves near T^* in Fig. 3 by a power $\Delta_{pg} \propto (x - x^*)^{\nu}$, with mean field critical exponent $\nu = 1/2$. It simultaneously satisfied the criticality condition (where $n_1 = n_2$):

$$1 = \frac{1}{NN'} \sum_{\mathbf{k}} \frac{U}{4x_{\mathbf{k}}} \left(\tanh \left[\frac{E_{\mathbf{k}}^+}{2T^*} \right] - \tanh \left[\frac{E_{\mathbf{k}}^-}{2T^*} \right] \right). \quad (\text{B6})$$

There is no experimental consensus on the shape of this line at small temperatures⁶⁸⁶⁹, while order of magnitude is consistent with tunneling experiments⁴⁴. In our model the low temperature segment, $T < T_c$, of the line exhibits a weak first order transition with small latent heat.

2. Underdoped

In 2D the Mermin - Wagner theorem⁷⁰ states that fluctuations for systems that have a continuous symmetry are strong enough to destroy long range order at any nonzero temperature. The order parameter locally exists, but averages out due to incoherence of its “phase” over the sample. A more rigorous approach would be to divide the degrees of freedom into two scales, large distance correlations, and short distance correlations. It can be performed for certain bosonic models using renormalization group ideas, especially when the Berezinskii - Kosterlitz - Thouless type transition is involved. However such an approach is complicated in fermionic models in which order parameter is quadratic in fermionic operators⁷¹. A much simpler symmetrization approach that does not involve the explicit separation of scales was proposed in ref.³⁹. It was demonstrated by comparing with determinantal Monte Carlo simulations and for small sizes to exact diagonalization that the symmetrization therefore qualitatively takes into account the largest available scale by “averaging over” the global symmetry group and agrees to within 5% with exact and MC results. We start with symmetrization of the HF Green function (GF). For (conserved) spin projection σ the GF on magnetic BZ is a 2×2 sublattice matrix,

$$G_{mk_1k_2}^\sigma = \frac{1}{x_{\mathbf{k}}^2 - (-i\omega_m + E'_{\mathbf{k}})^2} \begin{pmatrix} -i\omega_m + E'_{\mathbf{k}} - (-1)^\sigma \Delta_{pg} & h_{\mathbf{k}}^* \\ h_{\mathbf{k}} & -i\omega_m + E'_{\mathbf{k}} + (-1)^\sigma \Delta_{pg} \end{pmatrix}, \quad (\text{B7})$$

where $E'_{\mathbf{k}} = \epsilon'_{\mathbf{k}} + \frac{U_r}{2}n - \mu$ and $\sigma = 0$ for \uparrow and 1 for \downarrow .

3. Symmetrization

The relation between the matrix on magnetic Brillouin zone and the symmetrized Matsubara Green's function on the whole BZ (nonmagnetic, since the symmetry is restored), $-\pi/a < k_x, k_y \leq \pi/a$ is³⁹,

$$G_{mk_xk_y}^{sym} = \frac{1}{4} \sum_{\sigma} \left(G_{m,k_x,k_x+k_y}^{\sigma AA} + e^{ik_x a} G_{m,k_x,k_x+k_y}^{\sigma AB} + e^{-ik_x a} G_{m,k_x,k_x+k_y}^{\sigma BA} + G_{m,k_x,k_x+k_y}^{\sigma BB} \right). \quad (\text{B8})$$

Here G^{IJ} are elements of the matrix of Eq.(B7). As a result the Green's function (after analytic continuation) is,

$$G^{sym}(\omega, \mathbf{k}) = \frac{1}{2} \left(\frac{Z_{\mathbf{k}}^+}{\omega + i\eta + E_{\mathbf{k}}^+} + \frac{Z_{\mathbf{k}}^-}{\omega + i\eta + E_{\mathbf{k}}^-} \right); \quad (\text{B9})$$

$$Z_{\mathbf{k}}^{\pm} = \epsilon_{\mathbf{k}} / \sqrt{\Delta_{pg}^2 + |\epsilon_{\mathbf{k}}|^2} \pm 1,$$

where $\epsilon_{\mathbf{k}}$ was defined in Eq.(5) and η is the damping parameter. The dispersion relation in the nonmagnetic basis takes a form

$$E_{\mathbf{k}}^{\pm} = \epsilon'_{\mathbf{k}} - \mu + U_r \frac{n}{2} \pm \sqrt{\Delta_{pg}^2 + |\epsilon_{\mathbf{k}}|^2}, \quad (\text{B10})$$

where $\epsilon_{\mathbf{k}}$ was defined in Eq.(5). This is quite similar to one obtained in the slave boson approach to the t-J⁷² and RVB⁵² approaches.

4. EPI in the magnetic Brillouin zone

The connection between the electron - electron attraction due to phonons given in Eq.(18) in the usual "paramagnetic" basis, that is full BZ (marked by \bar{v}_{k_x, k_y} here) in the underdoped cases should be represented as a matrix elements in the sublattice space defined on a smaller magnetic BZ. The matrix,

$$v_{k_1 k_2}^{ph} = \frac{1}{2} \begin{pmatrix} \bar{v}_{k_1, k_2 - k_1} + \bar{v}_{k_1 + \pi, k_2 - k_1 + \pi} & (\bar{v}_{k_1, k_2 - k_1} - \bar{v}_{k_1 + \pi, k_2 - k_1 + \pi}) \exp[-iak_1] \\ (\bar{v}_{k_1, k_2 - k_1} - \bar{v}_{k_1 + \pi, k_2 - k_1 + \pi}) \exp[iak_1] & \bar{v}_{k_1, k_2 - k_1} + \bar{v}_{k_1 + \pi, k_2 - k_1 + \pi} \end{pmatrix}, \quad (\text{B11})$$

was used to calculate the phonon effects in both normal and superconducting state.

5. Susceptibility

The susceptibility matrix that enters the effective electron - electron interaction strength due to (the Hubbard repulsion induced) correlations is calculated in the post-Gaussian approximation as Lindhard type diagrams given in Fig.11. They are similar to the paramagnetic case⁵⁹³⁸. The propagators of the diagrams however, Eq.(B7), are defined on magnetic BZ and have two sublattice indices. The spin singlet pairing contribution to elements comes from the left and center diagrams:

$$\begin{aligned}\chi_{m,\mathbf{q}}^{II} &= \frac{T}{NN'} \sum_{n\mathbf{p}} \left(-G_{m+n,\mathbf{q}+\mathbf{p}}^{\downarrow II} G_{n\mathbf{p}}^{\downarrow II} + G_{m+n,\mathbf{q}+\mathbf{p}}^{\uparrow II} G_{n\mathbf{p}}^{\uparrow II} \right); \\ \chi_{l,\mathbf{q}}^{AB} &= -\frac{T}{NN'} \sum_{n\mathbf{p}} \left(-G_{m+n,\mathbf{q}+\mathbf{p}}^{\downarrow AB} G_{n\mathbf{p}}^{\downarrow BA} + G_{m+n,\mathbf{q}+\mathbf{p}}^{\downarrow AB} G_{n\mathbf{p}}^{\uparrow BA} \right); \\ \chi_{l,\mathbf{q}}^{BA} &= \chi_{-l,-\mathbf{q}}^{AB*},\end{aligned}\tag{B12}$$

where $N' = N/2$ and $I = A, B$. The third diagram vanishes.

Summing up over integers n , one obtains

$$\begin{aligned}\chi_{m\mathbf{q}}^{AA} &= P_{m\mathbf{q}} - Q_{m\mathbf{q}}; \\ \chi_{m\mathbf{q}}^{AB} &= R_{m\mathbf{q}}; \\ \chi_{m\mathbf{q}}^{BB} &= -P_{m\mathbf{q}} - Q_{m\mathbf{q}},\end{aligned}\tag{B13}$$

where

$$\begin{aligned}P_{m\mathbf{q}} &= \frac{1}{2NN'} \sum_{\mathbf{p}} \left(L_m [E_{\mathbf{p}}^-, E_{\mathbf{q}+\mathbf{p}}^-] + L_m [E_{\mathbf{p}}^-, E_{\mathbf{q}+\mathbf{p}}^+] + L_m [E_{\mathbf{p}}^+, E_{\mathbf{q}+\mathbf{p}}^-] + L_m [E_{\mathbf{p}}^+, E_{\mathbf{q}+\mathbf{p}}^+] \right); \\ Q_{m\mathbf{q}} &= \frac{\Delta_{pg}}{NN'} \sum_{\mathbf{p}} \frac{1}{x_{\mathbf{p}}} \left(L_m [E_{\mathbf{p}}^+, E_{\mathbf{q}+\mathbf{p}}^-] - L_m [E_{\mathbf{p}}^-, E_{\mathbf{q}+\mathbf{p}}^+] + L_m [E_{\mathbf{p}}^+, E_{\mathbf{q}+\mathbf{p}}^+] - L_m [E_{\mathbf{p}}^-, E_{\mathbf{q}+\mathbf{p}}^-] \right); \\ R_{m\mathbf{q}} &= \frac{1}{2NN'} \sum_{\mathbf{p}} \frac{h_{\mathbf{q}+\mathbf{p}}^* h_{\mathbf{p}}}{x_{\mathbf{q}+\mathbf{p}} x_{\mathbf{p}}} \left(L_m [E_{\mathbf{p}}^-, E_{\mathbf{q}+\mathbf{p}}^+] + L_m [E_{\mathbf{p}}^+, E_{\mathbf{q}+\mathbf{p}}^-] - L_m [E_{\mathbf{p}}^+, E_{\mathbf{q}+\mathbf{p}}^+] - L_m [E_{\mathbf{p}}^-, E_{\mathbf{q}+\mathbf{p}}^-] \right).\end{aligned}\tag{B14}$$

Here

$$L_m [E_1, E_2] = \frac{f_F [E_1] - f_F [E_2]}{2i\pi T m + E_1 - E_2},\tag{B15}$$

Δ_{pg} is the pseudogap energy, $x_{\mathbf{p}}$ is defined in Eq.(B5), $E_{\mathbf{p}}^{\pm}$ in Eq.(B4) and $h_{\mathbf{p}}$ in Eq.(B2).

6. Kink in dispersion relation (overdoped)

The calculation is similar to that for the simpler paramagnetic case. The result is:

$$\begin{aligned}\frac{d}{d\omega} I_{\omega,\mathbf{p}} &= \frac{Z^+}{2} \left(\frac{f_B [\Omega] - f_F [-E_{\mathbf{k}+1}^+] + 1}{(\omega + i\eta + \Omega - E_{\mathbf{k}+1}^+)^2} + \frac{f_B [\Omega] + f_F [-E_{\mathbf{k}+1}^+]}{(\omega + i\eta - \Omega - E_{\mathbf{k}+1}^+)^2} \right) \\ &\quad + \frac{Z^-}{2} \{E^+ \rightarrow E^-\},\end{aligned}\tag{B16}$$

where the energies E^{\pm} and Z^{\pm} were defined in Eq.(B9,B10).

Appendix C: C. Gap equation in underdoped system

1. Derivation

We derive the Gorkov's equations within the functional integral approach⁷³ starting from the effective electron action for grassmanian fields $\psi_{\mathbf{k},n}^{*\sigma}$ and $\psi_{\mathbf{k},n}^{\sigma}$. To simplify the presentation it is useful to lump the quasi - momentum and

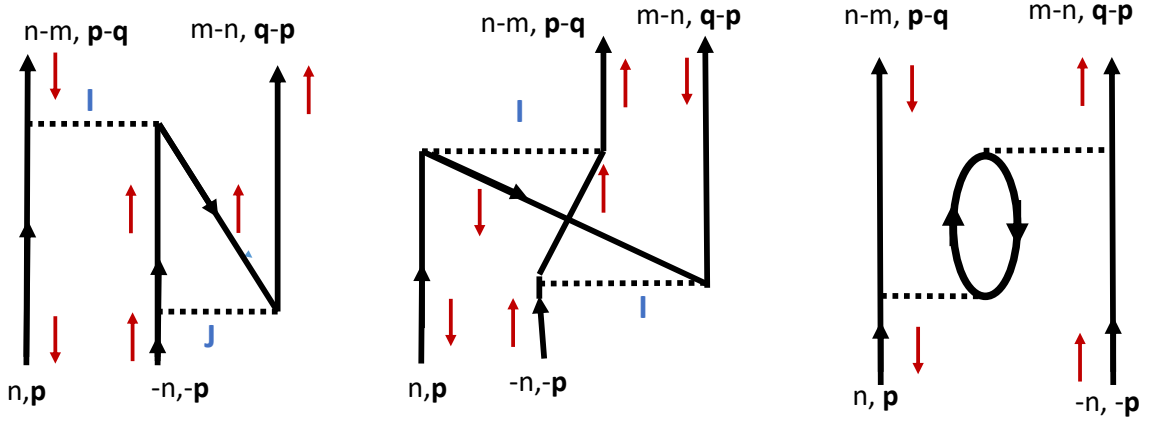


FIG. 11. Three second order diagrams determining the effective electron - electron interaction due to spin fluctuations. Both spin and sublattice indices are indicated. While the diagram on left and center give nonzero contributions of Eq.(B12), the third vanishes due to conflict in assigning spin indices to propagators in the loop.

the Matsubara frequency into a single subscript, $\{n, k_1, k_2\} \rightarrow \alpha$, and the spin and sublattice into the four component spinor $\{\sigma, I\} \rightarrow a$. The action of Eq.(24) takes a standard multicomponent four - Fermi form studied for example in ref.¹⁷:

$$\mathcal{A}[\psi] = \psi_\alpha^{*a} T_\alpha^{ab} \psi_\alpha^b + \frac{1}{2} \psi_\beta^{*a} \psi_{\chi+\beta}^a v_{-\chi}^{ab} \psi_\gamma^{*b} \psi_{\gamma-\chi}^b. \quad (\text{C1})$$

The hopping 4×4 matrix (inverse GF) for $a = \{\sigma, I\}$, $b = \{\rho, J\}$ in the following form,

$$T_{\{n, k_1, k_2\}}^{ab} = \begin{pmatrix} \delta^{\sigma\rho} (-i\omega_n + \varepsilon'_k - \mu + \frac{U_r n}{2}) + \sigma_z^{\sigma\rho} \Delta_{pg} & -\delta^{\sigma\rho} h_k^* \\ -\delta^{\sigma\rho} h_k & \delta^{\sigma\rho} (-i\omega_n + \varepsilon'_k - \mu + \frac{U_r n}{2}) - \sigma_z^{\sigma\rho} \Delta_{pg} \end{pmatrix}, \quad (\text{C2})$$

with I and J being the row and the column indices.

Gorkov equations in matrix form are:

$$\begin{aligned} -G_\alpha T_\alpha - F_\alpha \Delta_\alpha^{*t} &= I; \\ G_\alpha \Delta_\alpha - F_\alpha T_{-\alpha}^t &= 0, \end{aligned} \quad (\text{C3})$$

where F_α is the anomalous GF and the matrix gap function is defined $[\Delta_\alpha]$ in components as (see Fig.12))

$$\Delta_\alpha^{bc} = \sum_\chi v_{\alpha-\chi}^{bc} F_\chi^{bc}. \quad (\text{C4})$$

The corresponding gap equation is

$$\Delta_\alpha^{bc} = - \sum_\chi v_{\alpha-\chi}^{bc} \left[\left(T_{-\chi}^t [\Delta_\chi]^{-1} T_\chi + \Delta_\chi^\dagger \right)^{-1} \right]^{bc}. \quad (\text{C5})$$

The singlet Ansatz Eq.(25) leads to Eq.(26).

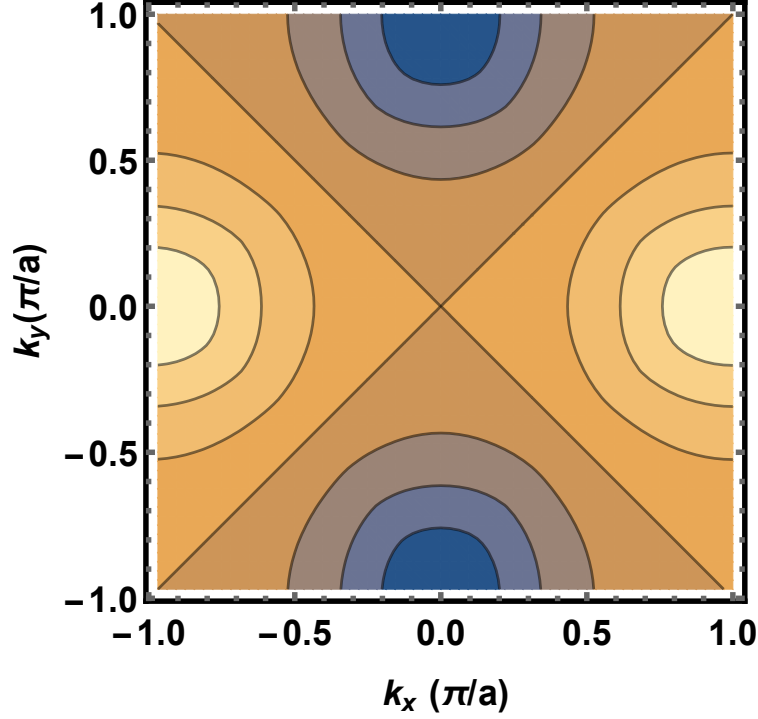


FIG. 12. The d - wave solution of the gap equation for optimal doping, $x = 0.166$ at $50K$.

2. The d -wave gap

The blue part of the surface corresponds to $x \geq x^{opt}$. The line of vanishing gap determines the critical temperature values on the phase diagram in Fig. 4 (red squares). In the optimal and overdoped domains it agrees well with the parabolic experimental dependence (dashed curve) taken from ref.¹⁸. If one neglects the magnon contribution, namely takes $v = v^{ph}$, the temperatures are lower by 15-20% (red circles).

One observes that the decrease of T_c is rather slow (linear) at large doping compared to the experiment. When doping becomes of order 30% it is expected to significantly impacts the effective mesoscopic lattice model parameters (μ, U, t, t'). In underdoped cases the pseudogap should be taken into account. The results are the yellow part of the surface in Fig.13 for the gap and critical temperatures shown on the left hand side of the phase diagram, Fig.3. The maximum gap as function of doping and temperature is given in Fig.13 (the yellow part of the surface).

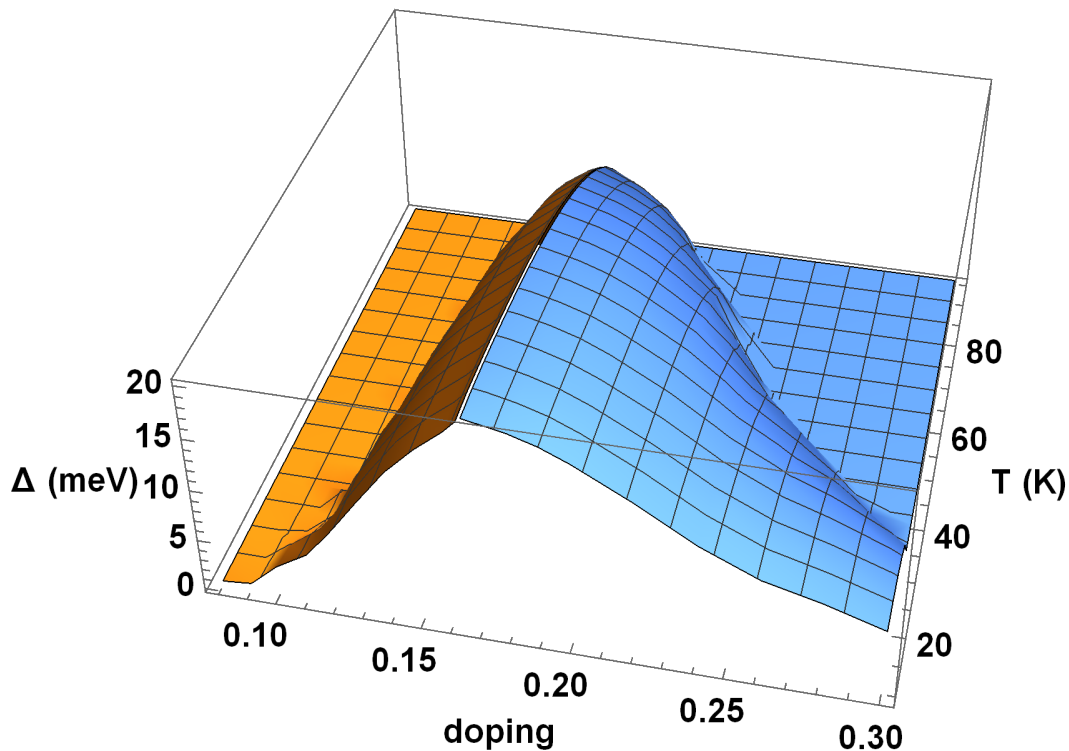


FIG. 13. Superconducting (maximal) d - wave Matsubara gap as function of dopings and temperatures. Underdoped parts are in brown, while the overdoped in blue.

-
- ¹ Timusk T. and Statt B. 1999 Rep. Prog. Phys. **62**, 61; Sadvskii M. V. Uspekhi 2001 Fiz. Nauk **171**, 539 [2001 Sov. Phys. Usp. **44**, 515].
- ² Dagotto E. 1994 Rev. Mod. Phys. **66**, 763; Lee P. A. , Nagaosa N. , and Wen X.-G., 2006 Rev. Mod. Phys. **78**, 17.
- ³ Liu D. et al. 2012 Nature Com. **3**, 931; He S. et al, Nature Mater. 2013 **12**, 605; Wang Q. , Zhang W. ,Zhang Z. , Sun Y. , Xing Y. , Wang Y. , Wang L. , Ma X. , Xue Q.-K. and Wang J. , 2015 2D Mater. **2** 044012; Huang D. and Hoffman J. F. , 2017 Ann. Rev. Cond. Mat. Phys. **8**, 311.
- ⁴ Zhang P. et al , 2016 Phys. Rev. B **94**, 104510.
- ⁵ Peng R. et al 2014 Nature Com. **5**, 5044; Ding H. , Lv Y.-F. ,Zhao K. , Wang W.-L. ,Wang L. ,Song C.-L. ,Chen X. ,Ma X.-C. and Xue Q.-K. . 2016 Phys. Rev. Lett.,**117**, 067001; Rebec S. N. , Jia T. , Zhang C. , Hashimoto M., Lu D.H. , Moore R. G. , and Shen Z.X. , 2017 Phys. Rev. Lett.,**118**, 067002.
- ⁶ Wang L. , Ma X. , and Xue Q. - K. , 2016 Supercond. Sci. Technol. **29**, 123001.
- ⁷ Fan Q. et al 2015 Nature Phys., **11**, 946; Tang C. et al 2016 Phys. Rev. B **93**, 020507(R).
- ⁸ Lee D. - H. 2015 Chinese Physics B **24** 117405.
- ⁹ Dai P. , Hu J, and Dagotto E. , 2012 Nat. Phys. **8**, 709.
- ¹⁰ Gorkov L. P. , 2016 Phys. Rev. B **93**, 054517, 060507(R); Rosenstein B. ,Shapiro B.Ya. , Shapiro I. , and Li D. , 2016 Phys. Rev. B **94**, 024505.
- ¹¹ Rademaker L. ,Wang Y. , Berlijn T. and Johnston T. , 2016 New J. Phys.**18**, 022001; Kulić M. L. and Dolgov O. V. , 2017 New J. Phys. **19** 013020.
- ¹² Song Q. et al, 2019 Nature Com. **10**, 758.

- ¹³ Zhang S. et al. 2016 Phys. Rev. B **94**, 081116(R).
- ¹⁴ Xiang Y. Y. , Wang F. , Wang D. , Wang Q. H. , and Lee D. H. 2012 Phys. Rev. B **86**, 134508; Wang Y. , Nakatsukasa K. , Rademaker L. , Berlijn T. and Johnston S. 2016 Supercond. Sci. Technol. **29**, 054009.
- ¹⁵ M. L. Kulić, 2000 Phys. Rep. **38**, 1 and references therein.
- ¹⁶ Lichtenstein A. I. and Kulic M. L. 1995 Physica C **245**, 186;
- ¹⁷ Rosenstein B. and Shapiro B. Ya. 2019 Phys. Rev. B **100**, 054514.
- ¹⁸ Sterpetti E. , Biscaras J. , Arb A. , Shukla A. 2017 Nat. Com. **8**, 2060.
- ¹⁹ Zhao S.Y. et al 2019 Phys. Rev. Let. **122**, 247001.
- ²⁰ Zhong Y. et al. 2016 Science Bull. **61**, 1239.
- ²¹ Zhu G.-Y. , Zhang F.-C. , and Zhang G.-M. 2016 Phys. Rev. B **94**, 174501; Jiang K. , Wu X. , Hu J. and Wang Z. 2018 Phys. Rev. Let. **121** 227002; Wang S. , Zhang L. Wang F. 2018 Phys. Rev. B **97**, 035112; Maier T. , Berlijn T. ,and Scalapino D. J. 2019 Phys. Rev. B **99**, 224515.
- ²² Bulut N. and Scalapino D. J. 1992 Phys. Rev. B **45**, 2371; Song J. and Annett J. F. 1995 Phys. Rev. B **51** 3840; Devereaux T. P.,Virosztek A. , and Zawadowski A. 1995 Phys. Rev. B **51**, 505; Nazarenko A. and Dagotto E. 1996 Phys. Rev. B **53**, R2987; Devereaux T. P. , Cuk T. , Shen Z.-X. , and Nagaosa N. 2004 Phys. Rev. Let. **93**, 117004; Honerkamp C. , Fu H.C. and Lee D.-H. 2007 Phys. Rev. B **75**, 014503.
- ²³ Conradson S. D. , Railstrick I. D. and Bishop A. I. , 1990 Science **248**, 1395; Frick M., Morgenstern I. and von der Linden W. , Z. 1991 Phys. B **82**, 339; Reedyk M., Timusk T. , Xue J. S., and Greedan J.E. 1994 Phys. Rev. B **49**, 15984.
- ²⁴ Huang Z. B. , Hanke W. , Arrigoni E. and Scalapino D. J. , 2003 Phys. Rev. B **68**, 220507(R); Vidmar L. , Bonca J. , Maekawa S. and Tohyama T. 2009 Phys. Rev. Let. **103**, 186401; Johnston S. , Vernay F. , Moritz B., Shen Z.-X. , Nagaosa N. , Zaanen J. , and Devereaux T. P. 2010 Phys. Rev. B **82**, 064513; Huang Z. B. , Lin H.-Q. and Arrigoni E. 2011 Phys. Rev. B **83** 064521.
- ²⁵ Slezak J. A. , Lee J. , Wang M. , McElroy K. , Fujita K. , Andersen B. M., Hirschfeld P. J. , Eisaki H., Uchida S. and Davis J. C. 2008 PNAS **105** 3203.
- ²⁶ Y. Y. Peng et al. 2017 Nature Phys. **13**, 1201.
- ²⁷ J. Lee et al Nature 2006 **442**, 546.
- ²⁸ P. V. Bogdanov, et al. 2000 Phys. Rev. Let. **85**, 2581; Kaminski A. , Randeria M., Campuzano J.C. , Norman M.R. , Fretwell H. , Mesot J. , Sato T., Takahashi T., Kadowaki K. 2001 Phys. Rev. Let. **86**, 1070; P. D. Johnson et al. 2001 Phys. Rev. Let. **87**, 177007; A. Lanzara, et al., 2001 Nature **412**, 510.
- ²⁹ Gweon G.-H. , Sasagawa D. , Zhou S. Y. , Graf J. , Tagaki H. , Lee D.-H. and Lanzara A. 2004 Nature **430** ,188.
- ³⁰ Iwasawa H. et al 2008 Phys. Rev. Let. **101**, 157005.
- ³¹ Franck J. P. , 1994 " *Experimental Studies of The Isotope Effect*" in " *High Temperature Superconductors: Physical Properties of High Temperature Superconductors IV*" Singapore, Ed D. M. Ginsberg, World Scientific; Malik M.A. and Malik B.A. , 2012 Am. J. Cond. Mat. Phys. **2**, 67.
- ³² Falter C. and Schnetgoke F. , 2002 Phys. Rev. B **65**, 054510; C. Falter, Phys. Stat. Sol. 2005 **242**, 78.
- ³³ A. A. Abrahamson, 1969 Phys. Rev. **178**, 76.
- ³⁴ Evarestov R. A. , 2012 Quantum Chemistry of Solids, Second Edition, London Springer Series in Solid-State Sciences **153**.
- ³⁵ Falter C. , Klenner M. and Chen Q. 1993 Phys. Rev. B **48**, 16690; Rashba E. I, Sherman 1988 E.Y. JETP Letters **47** 482.
- ³⁶ Nilsson F. , Karlsson K. and Aryasetiawan F., 2019 Phys. Rev. B **99**, 075135.
- ³⁷ Jang S. W. , Sakakibara H. , Kino H. , Kotani T. , Kuroki K. and Han M. J. 2016 Scientific Rep. **6**, 33397.
- ³⁸ Rømer A. T. , Maier T. A., Kreisel A. , Eremin I., Hirschfeld P. J. , Andersen B. M. 2020 Phys. Rev. Research **2**, 013108.
- ³⁹ Rosenstein B., Li D., Ma T. X. and Kao H.C. 2019 Phys. Rev. B **100**, 125140.
- ⁴⁰ McMillan W. L. 1968 Phys. Rev. **167** 331.
- ⁴¹ Annett J. F. and Martin R. M. 1990 Phys. Rev. B **42** 3929.
- ⁴² Mahan G. G. 2011 Condensed Matter in a Nutshell, Princeton, Princeton University Press.
- ⁴³ Kordyuk A. A., Borisenko S. V., Knupfer M. and Fink J. 2003 Phys. Rev. B **67**, 064504; Markiewicz R. S., Sahrakorpi S., Lindroos M., Lin H. and Bansil A. 2005 Phys. Rev. B **72**, 054519.
- ⁴⁴ Jacobs Th. ,Simsek Y., Koval Y., Müller P. and Krasnov V. M. , 2016 Phys. Rev. Let. **116**, 067001.
- ⁴⁵ Lee J. J et al 2014 Nature **515** 245.
- ⁴⁶ Timirgazin M. A., Igoshev P. A., Arzhnikov A. K. and Yu. V. Irhin, 2016 J. Low Temp. Phys. **185**, 651.
- ⁴⁷ Y. G. Zhong et al. 2018 Phys. Rev. B **98**, 140507(R).
- ⁴⁸ Seki K and Sorella S. 2019 Phys. Rev. B **99** 144407.
- ⁴⁹ Rohringer G., Hafermann H., Toschi A., Katanin A. A. ,Antipov A. E., Katsnelson M. I., Lichtenstein A. I., Rubtsov A. N. and Held K. 2018 Rev. Mod. Phys. **90** 025003.
- ⁵⁰ Pudleiner P., Kauch A., Held K. and Li G. 2019 Phys. Rev. B **100**, 075108.
- ⁵¹ Maier, T.A., Macridin, T.A., Jarrell, M., Scalapino, D.J. 2007 Phys. Rev. B **76** 144516.
- ⁵² Yang K. Y. , Rice T. M. and Zhang F. C. 2006 Phys. Rev. B **73**, 174501; Rice T. M., Yang K.-Y. and Zhang F. C. 2012 Rep. Prog. Phys. **75**, 016502.
- ⁵³ Hufner S., Hossain M. A., Damascelli A. and Sawatzky G. A. , 2008 Rep. Prog. Phys. **71**, 062501 and references therein; Ren J. K., Zhu X. B., Yu H. F., Tian Y., Yang H. F. , Gu C. Z., Wang N. L., Ren Y. F. and Zhao S. P. 2012 Sci. Rep. **2**, 248; Mukhopadhyay S. et al., 2019 PNAS **116**, 13249.
- ⁵⁴ Reiss J., Rohe D., and Metzner W. 2007 Phys. Rev. B **75**, 075110; Eberlein A. and Metzner W. 2014 Phys. Rev. B **89**, 035126.
- ⁵⁵ Yang H.-B., Rameau J. D., Pan Z.-H., Gu G. D., Johnson P. D., Claus H., Hinks D. G. and Kidd T. E. 2011 Phys. Rev.

- Let. **107** 047003.
- ⁵⁶ He Y. et al. 2018 Science **362**, 62.
- ⁵⁷ Dahm T. , Hinkov V., Borisenko S. V., Kordyuk A. A., Zabolotny V. B., Fink J., Büchner B., Scalapino D. J., Hanke W. and Keimer B. 2009 Nat. Physics **5** 217.
- ⁵⁸ Misuno R., Ochi M. and Kuroki K. 2017 J. Phys. Soc. Jap. **86**, 114706; Taheridehkordi A., Curnoe S. H. and LeBlanc J. P. F., 2020 Phys. Rev. B **102**, 045115.
- ⁵⁹ Kohn W. and Luttinger J. M., 1965 Phys. Rev. Let. **15**, 526.
- ⁶⁰ Zhao G. M., Hunt M.B., Keller H. , Muller K.A. 1997 Nature **358**, 236; Zhao G. M., Keller H., Muller K.A. J. Phys. Cond. Mat. 1998 **10** 9055.
- ⁶¹ Zech D., Keller H., Conder K., Kaldis E. , Liarokapis E., Poulakis N., Muller K.A. 1994 Nature **371**, 681; Keller H. 2005 in "Superconductivity in Complex Systems", **114**, edited by Muller K. and Bussmann-Holder A., Berlin Heidelberg, Springer
- ⁶² Rosenstein B. and Li D.P. 2010 Rev. Mod. Phys. **82**, 109.
- ⁶³ Feiner L. F. ,Jefferson J. H. andRaimondi R. 1996 Phys. Rev. B **53**, 8751.
- ⁶⁴ Zhang F. C. andRice T. M. , 1988 Phys. Rev. B **37**, 3759.
- ⁶⁵ Davydov A. , 1980 *Theory of Solids*, Moscow Nauka.
- ⁶⁶ Lin H. Q. and Hirsch J. E. 1987 Phys. Rev. B **35**, 3359;Igoshev P. A. ,Timirgazin M. A. , Katanin A. A.,Arzhnikov A. K. , and Irkhin V. Yu. 2010 Phys. Rev. B **81** 094407;Igoshev P. A. , Timirgazin M. A. ,Gilmutdinov V. F. ,Arzhnikov A. K. and Irkhin V. Yu. 2015 J. Phys. Cond. Mat. **27** 446002.
- ⁶⁷ Langmann E and Wallin M., 2007 J. Stat. Physics **127** 825.
- ⁶⁸ Tallon J. L., Storey J. G. , Cooper J. R. , Loram J. W. 2020 Phys. Rev. B **101**, 174512.
- ⁶⁹ Frachet M. et al 2019 *Hidden magnetism at the pseudogap critical point of a high temperature superconductor*, arXiv:1909.10258.
- ⁷⁰ Chaikin P. M. and Lubensky T. C. ,1995 *Principles of Condensed Matter Physics*, Cambridge, Cambridge University Press.
- ⁷¹ Metzner W. and Yamase H. 2019 Phys. Rev. B **100**, 014504.
- ⁷² Izyumov Yu. A. 1999 Sov. Phys. Usp. **42**, 215 and references therein; Yamaji Y. and Imada M. 2011 Phys Rev B **83**, 214522.
- ⁷³ Negele J. W. and Orland H. , 1998 *Quantum Many-particle Systems*, London, Perseus Books, ; Li D., Rosenstein B., Shapiro B. Ya. and Shapiro I. 2015 Frontiers Phys., **10**, 303.